

# Comparison of Th, Sr, Nd and Pb isotopes in oceanic basalts: Implications for mantle heterogeneity and magma genesis

K.W.W. Sims\*, S.R. Hart

*Department of Geology and Geophysics, Woods Hole Oceanographic Institution, Woods Hole, MA 02543, United States*

Received 10 August 2005; received in revised form 7 February 2006; accepted 18 February 2006

Available online 24 April 2006

Editor: K. Farley

## Abstract

We report U–Th disequilibria data for a suite of 13 young basaltic samples from the Samoan Islands, which represent the end-member mantle component EM2, and 4 historic lavas from Mt. Erebus, typifying young HIMU. The Samoan samples have low  $^{230}\text{Th}/^{232}\text{Th}$  and  $^{238}\text{U}/^{232}\text{Th}$ , consistent with the enriched nature (EM2) of the Samoan mantle source, whereas the Mt. Erebus samples have high  $^{206}\text{Pb}/^{204}\text{Pb}$  and intermediate  $(^{230}\text{Th}/^{232}\text{Th})$  and  $(^{238}\text{U}/^{232}\text{Th})$ . When considered in the context of the global oceanic basalt database, the Samoan samples' low  $^{230}\text{Th}/^{232}\text{Th}$  and  $^{238}\text{U}/^{232}\text{Th}$  greatly extend the global correlations between  $^{230}\text{Th}/^{232}\text{Th}$  and  $^{238}\text{U}/^{232}\text{Th}$  with  $^{87}\text{Sr}/^{86}\text{Sr}$  and  $^{143}\text{Nd}/^{144}\text{Nd}$  and change the functional form of these correlations from linear to hyperbolic. Using a maximum likelihood non-linear inversion method, we show that these correlations of  $^{230}\text{Th}/^{232}\text{Th}$  and  $^{238}\text{U}/^{232}\text{Th}$  with  $^{87}\text{Sr}/^{86}\text{Sr}$  and  $^{143}\text{Nd}/^{144}\text{Nd}$  can be approximated by two-component mixing. However, the global oceanic basalt data also show considerable scatter about the best-fit mixing curves. This scatter is attributed to additional source components and melting processes influencing the lavas ( $^{230}\text{Th}/^{232}\text{Th}$ ) and ( $^{238}\text{U}/^{232}\text{Th}$ ). Additional source components are supported by the Pb isotope data, which clearly require more than two endmember mantle components. We also show that the extent and variability in ( $^{230}\text{Th}/^{238}\text{U}$ ) decreases as a function of source enrichment, with “depleted” MORB showing the largest extents and greatest variability in ( $^{230}\text{Th}/^{238}\text{U}$ ) and “enriched” OIB, like Samoa, showing smaller extents and less variability of ( $^{230}\text{Th}/^{238}\text{U}$ ). We interpret this observation in terms of differences in the melting regimes beneath mid-ocean ridges and ocean islands.

© 2006 Elsevier B.V. All rights reserved.

*Keywords:* U-series; Nd; Sr and Pb isotopes; mantle source heterogeneity; Magmagenesis; MORB; OIB

## 1. Introduction

Isotopic ratios measured in basaltic lavas provide a means to trace time-integrated variations of parent/daughter trace element ratios in mantle sources. The timescale over which these isotopic tracers respond to changes in the parent/daughter ratio is directly proportional to the half-life of the parent isotope. Most

radiogenic isotope tracers (e.g. Sr, Nd, Hf and Pb) have parent half-lives of 0.7–106 Ga and respond to changes in parent/daughter ratios (e.g. Rb/Sr, Sm/Nd, Lu/Hf) over timescales comparable to mantle convection. The  $^{230}\text{Th}/^{232}\text{Th}$  isotopic system, however, is intrinsically different — the half-life of daughter isotope  $^{230}\text{Th}$  is only 75 ka, and its abundance, relative to parent  $^{238}\text{U}$ , is determined by the radioactive principles governing U decay-series systematics. As a result, after 300 ka the Th isotopic composition of the mantle source directly reflects its  $^{238}\text{U}/^{232}\text{Th}$  source ratio.

\* Corresponding author.

E-mail address: [ksims@whoi.edu](mailto:ksims@whoi.edu) (K.W.W. Sims).

In principle, comparison of  $^{230}\text{Th}/^{232}\text{Th}$ ,  $^{238}\text{U}/^{232}\text{Th}$  and  $^{230}\text{Th}/^{238}\text{U}$  with longer-lived radiogenic isotopes (e.g.  $^{87}\text{Sr}/^{86}\text{Sr}$ ) can provide first-order insight into both the nature of the mantle source [1–4] and the styles of melt generation and magma transport [5–11]. While there are several studies comparing Th isotopes with longer-lived radiogenic isotopes in oceanic basalts, of the four mantle components (DMM, HIMU, EM1 and EM2) defining the mantle tetrahedron [12,13], depleted MORB mantle (DMM) is the only end-member component “well characterized” in its Th isotopic composition by high-precision mass spectrometric methods. Because of a lack of high quality Th isotopic measurements for the other three end-member mantle components (HIMU, EM1 and EM2), the form and relative significance of the relationships between  $^{230}\text{Th}/^{232}\text{Th}$ ,  $^{238}\text{U}/^{232}\text{Th}$  and  $^{230}\text{Th}/^{238}\text{U}$ , and the longer-lived radiogenic isotopes (i.e.  $^{87}\text{Sr}/^{86}\text{Sr}$ ,  $^{143}\text{Nd}/^{144}\text{Nd}$ ,  $^{208}\text{Pb}/^{204}\text{Pb}$ ,  $^{207}\text{Pb}/^{204}\text{Pb}$ ,  $^{206}\text{Pb}/^{204}\text{Pb}$  and) are not yet well defined.

Here we present new U–Th disequilibria data for a suite of thirteen young basaltic samples from the Samoan Islands and a suite of four historic ‘bomb’ samples from Mt. Erebus, Antarctica. The Samoan Islands represent the end-member “EM2” enriched mantle component and are characterized by radio-

genic  $^{87}\text{Sr}/^{86}\text{Sr}$ , unradiogenic  $^{143}\text{Nd}/^{144}\text{Nd}$ , and low to moderate  $^{206}\text{Pb}/^{204}\text{Pb}$  [14]. The Mt. Erebus samples are “HIMU” having intermediate  $^{87}\text{Sr}/^{86}\text{Sr}$ , intermediate  $^{143}\text{Nd}/^{144}\text{Nd}$ , and radiogenic  $^{206}\text{Pb}/^{204}\text{Pb}$ . While Mt. Erebus does not represent the end-member mantle component HIMU, there are no samples young enough for U–Th disequilibria studies from Mangai-Tubai (the HIMU end-member).

These new data are then compared with the MORB and OIB database for which U–Th disequilibria and longer-lived radiogenic isotopes of Sr, Nd, and Pb have been measured by mass spectrometric methods.

## 2. Comparison of ( $^{230}\text{Th}/^{232}\text{Th}$ ) and ( $^{238}\text{U}/^{232}\text{Th}$ ) with Sr, Nd and Pb isotopes in the global oceanic database

### 2.1. ( $^{230}\text{Th}/^{232}\text{Th}$ ) and ( $^{238}\text{U}/^{232}\text{Th}$ )

U and Th isotopes and concentrations have now been measured in several oceanic basalt suites by mass spectrometric methods, including MORB [5,10,11,15–25], Samoa [this work], Mt. Erebus [this work], Hawaii [5,10,26,27], Iceland [28,29], Canaries [30–32], and the Azores [33–35] (Fig. 1).

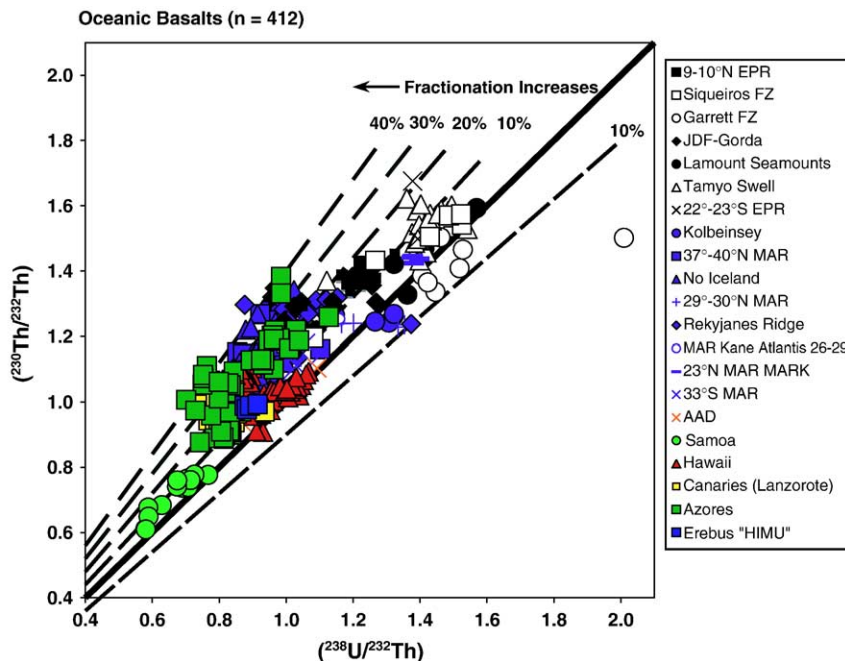


Fig. 1. ( $^{230}\text{Th}/^{232}\text{Th}$ ) versus ( $^{238}\text{U}/^{232}\text{Th}$ ) for our global compilation of literature data for mid-ocean ridge and ocean island basalts measured by mass spectrometric methods [5,10,11,15–27], Iceland [28,29], Canaries [30–32], and the Azores [33–35]. These data have been filtered to eliminate samples of uncertain eruption age, or which have been identified in the publishing study as altered by secondary, post-eruptive processes. Note that the new Mt. Erebus samples are historic, and the new Samoan samples are demonstrably young based upon historical constraints, or measurement of  $^{230}\text{Th}$ – $^{226}\text{Ra}$ – $^{210}\text{Pb}$  and  $^{210}\text{Po}$  disequilibria (Sims et al., in preparation).

The Samoan samples (Tables 1 and 2) have the lowest  $^{230}\text{Th}/^{232}\text{Th}$  and  $^{238}\text{U}/^{232}\text{Th}$  yet measured in oceanic basalts, consistent with the enriched nature of their mantle source. MORB, on the other hand, have high ( $^{230}\text{Th}/^{232}\text{Th}$ ) and  $^{238}\text{U}/^{232}\text{Th}$ , consistent with the depleted character of the MORB mantle source. The historic Mt. Erebus samples show intermediate ( $^{230}\text{Th}/^{232}\text{Th}$ ) and ( $^{238}\text{U}/^{232}\text{Th}$ ) consistent with their intermediate  $^{87}\text{Sr}/^{86}\text{Sr}$  and  $^{143}\text{Nd}/^{144}\text{Nd}$ . This global variation in ( $^{230}\text{Th}/^{232}\text{Th}$ ) and ( $^{238}\text{U}/^{232}\text{Th}$ ) is consistent with the correlation observed between Sr and Nd isotopes and supports the idea that the depleted mantle is complementary, at least in part, to the more enriched continental crust.

For the current global oceanic database ( $n=412$ ), the variability of  $^{230}\text{Th}/^{238}\text{U}$  is much smaller than the range of both ( $^{230}\text{Th}/^{232}\text{Th}$ ) and ( $^{238}\text{U}/^{232}\text{Th}$ ) (Fig. 1). Most oceanic basalts lie to the left of the equiline; this is interpreted as an indication of deep melting either in the presence of garnet or near solidus pyroxene at 1.5 GPa [36–39]. For the few oceanic basalts lying to the right of the equiline (Kolbeinsey Ridge and Garret Fracture Zone), these samples'  $^{238}\text{U}$  excesses are thought to indicate shallow melting of depleted peridotite [23,24].

The number of oceanic samples for which both U–Th isotopes and long-lived radiogenic isotopes have been measured by mass spectrometry is more limited. In the following, we evaluate the relationships between U–Th systematics and Sr isotopes ( $n=210$ ), Nd isotopes ( $n=161$ ), and Pb isotopes ( $n=147$ ) for the current global oceanic database.

## 2.2. Correlations of ( $^{238}\text{U}/^{232}\text{Th}$ ) and ( $^{230}\text{Th}/^{232}\text{Th}$ ) with $^{87}\text{Sr}/^{86}\text{Sr}$ : two-component mixing?

Early studies comparing  $^{230}\text{Th}/^{232}\text{Th}$  and  $^{87}\text{Sr}/^{86}\text{Sr}$  for MORB and OIB [1–4,7] observed a negative, linear correlation, which was interpreted as indicating that the U/Th of the mantle source (as inferred from the lavas' ( $^{230}\text{Th}/^{232}\text{Th}$ )) is a long-lived feature, consistent with the mantle Rb/Sr (as inferred from the lavas'  $^{87}\text{Sr}/^{86}\text{Sr}$ ).

The Samoan samples' low  $^{230}\text{Th}/^{232}\text{Th}$  and high  $^{87}\text{Sr}/^{86}\text{Sr}$  (up to 0.7089) greatly extend this global correlation and show that its functional form is hyperbolic rather than linear (Fig. 2A). When this hyperbolic trend is interpreted as reflecting a binary mixing line, its curvature indicates that the Th/Sr ratio in the enriched

Table 1  
 $^{143}\text{Nd}/^{144}\text{Nd}$ ,  $^{87}\text{Sr}/^{86}\text{Sr}$ ,  $^{208}\text{Pb}/^{204}\text{Pb}$ ,  $^{207}\text{Pb}/^{204}\text{Pb}$  and  $^{206}\text{Pb}/^{204}\text{Pb}$  [14,61,62] for Samoan and Mt. Erebus samples

	$^{87}\text{Sr}/^{86}\text{Sr}$	$^{143}\text{Nd}/^{144}\text{Nd}$	Epsilon Nd	$^{208}\text{Pb}/^{204}\text{Pb}$	$^{207}\text{Pb}/^{204}\text{Pb}$	$^{206}\text{Pb}/^{204}\text{Pb}$
<i>Samoa</i>						
63-13	0.705520	0.512716	1.5	39.699	15.624	19.352
68-30	0.705215	0.512734	1.9	39.589	15.615	19.332
70-1	0.705371	0.512768	2.5	39.641	15.608	19.371
70-9	0.705352	0.512753	2.2	39.683	15.619	19.386
71-2	0.705943	0.512743	2.0	39.680	15.605	19.332
72-2	0.705395	0.512740	2.0	39.657	15.604	19.365
73-1	0.706720	0.512669	0.6	39.585	15.617	19.215
73-3	0.705616	0.512711	1.4	39.638	15.602	19.328
73-12	0.706653	0.512686	0.9	39.529	15.600	19.195
76-1	0.707192	0.512637	0.0	39.847	15.636	19.338
77-9	0.707260	0.512579	−1.2	39.853	15.635	19.331
78-1	0.708901	0.512521	−2.3	39.862	15.647	19.237
SAV B6	0.705786	0.512716	1.5	39.121	15.610	18.785
<i>Mt. Erebus</i>						
ER 83220	0.703039	0.512908	5.3	39.515	15.649	19.946
ER-84505	0.703133	0.512906	5.2	39.489	15.648	19.916
ER 97KS	0.703033	0.512911	5.3	39.509	15.648	19.941
ER 2000	0.703043	0.512905	5.2	39.508	15.648	19.939

(1) Samoan data from Workman et al [14].

(2) For Mt Erebus samples Pb, Sr and Nd isotopes measured at WHOI by PIMMS using the ThermoFinnigan NEPTUNE. Data are reported relative to 0.71024 (NBS 987) and 0.511847 (La Jolla), respectively. Based upon replicate analysis of NBS SRM 987 and La Jolla Nd isotopic standard,  $2\sigma$  precisions for Sr and Nd isotope data are  $\pm 26$  ppm and  $\pm 15$  ppm, and  $\epsilon_{\text{Nd}}$  values calculated using ( $^{143}\text{Nd}/^{144}\text{Nd}$ )<sub>Chur(0)</sub> = 0.512638. Measured Pb isotope ratios are normalized to both an internal Tl std and then to NBS 981 using the values of Todt et al. [61]. For these measurements, every two samples are interspersed with an analyses of NBS 960 for the mass bias correction [62]. Based upon replicate analyses of NBS981  $2\sigma$  errors for  $^{208}\text{Pb}/^{204}\text{Pb}$ ;  $^{207}\text{Pb}/^{204}\text{Pb}$  and  $^{206}\text{Pb}/^{204}\text{Pb}$  are 110–150 ppm ( $2\sigma$ ) and 90 ppm ( $2\sigma$ ) for  $^{208}\text{Pb}/^{206}\text{Pb}$ .

Table 2  
[Th], [U], ( $^{230}\text{Th}/^{232}\text{Th}$ ), ( $^{238}\text{U}/^{232}\text{Th}$ ) and ( $^{230}\text{Th}/^{238}\text{U}$ ) U for Samoan and Mt. Erebus samples

Sample	[Th] $\mu\text{g/g}$	[U] $\mu\text{g/g}$	Th/U	( $^{238}\text{U}/^{232}\text{Th}$ )	( $^{230}\text{Th}/^{232}\text{Th}$ )	( $^{230}\text{Th}/^{238}\text{U}$ )	( $^{234}\text{U}/^{238}\text{U}$ )
63-13 (avg)	4.99	1.13	4.40	0.689	0.737	1.07	1.003
68-30 (avg)	3.52	0.82	4.31	0.705	0.763	1.09	1.004
70-1	3.96	1.00	3.96	0.767	0.777	1.01	1.007
70-9 (avg)	4.20	1.0	4.20	0.721	0.757	1.05	1.005
71-2 (avg)	2.30	0.54	4.29	0.707	0.733	1.04	1.005
72-2 (avg)	5.15	1.21	4.25	0.714	0.757	1.06	1.001
73-1 (avg)	6.00	1.24	4.83	0.628	0.677	1.08	1.004
73-3 (avg)	4.83	1.07	4.50	0.674	0.735	1.09	1.003
73-12 (avg)	5.07	0.98	5.16	0.588	0.675	1.15	1.005
76-1	6.37	1.22	5.24	0.579	0.611	1.05	
77-9	6.68	1.30	5.15	0.589	0.649	1.10	
78-1 (avg)	5.79	1.10	5.26	0.577	0.598	1.04	1.004
SAV B6 (avg)	3.34	0.74	4.50	0.675	0.763	1.13	1.002
83220	30.93	8.94	3.46	0.877	0.985	1.12	1.001
ER-84505	29.54	8.43	3.51	0.865	0.976	1.13	1.002
ER 97KS	32.16	9.27	3.47	0.874	0.989	1.13	1.001
ER 2000	32.19	9.19	3.50	0.866	0.989	1.14	1.002

The Mt. Erebus samples are historic, whereas the Samoan samples young ages are established by measurements of  $^{230}\text{Th}$ – $^{226}\text{Ra}$ – $^{210}\text{Pb}$  and  $^{210}\text{Po}$  disequilibria [63] (Sims et al., in preparation).

(1) Samoan and Mt Erebus samples represent replicate averages. Samples were hand-picked under a microscope, then ultrasonically leached in sequential treatments of 0.1N HCL plus 2% $\text{H}_2\text{O}_2$  (15 min), DI water (twice, each time for 15 min), 0.1N oxalic acid plus 2%  $\text{H}_2\text{O}_2$ , DI water (twice, each time for 15 min), acetone (15 min). Samples were then hand-picked by microscope for a second time and then lightly leached in the clean lab in 0.1N HCL plus 2% $\text{H}_2\text{O}_2$  (15 min) using ultra-pure reagents. Sample splits ( $>1$  g) were then dissolved, aliquoted, spiked and then U–Th–Pa were separated using chemical techniques outlined in Refs. [10,11,16,17]. Note that measurements of TML, leached under similar conditions, show that this leaching procedure does not alter the samples U and Th concentrations.

(2) [U], [Th], measured by ID-ICPMS at WHOI using the ThermoFinnigan ELEMENT2. Measurement errors ( $2\sigma$ ) range from 0.1% to 0.9% and reproducibility for these samples is less than 1.1% ( $2\sigma$ ). Replicate measurements of [U], [Th] in rock standards ATHO ( $n=10$ ) and TML ( $n=8$ ) yield for ATHO [U]= $2.235\pm 0.009$  and [Th]= $7.45\pm 0.06$ ; and TML [U]= $10.6\pm 0.1$  and [Th]= $29.84\pm 0.04$ .

(3) ( ) denotes activity  $\lambda_{238}=1.551\times 10^{-10}\text{ yr}^{-1}$ ;  $\lambda_{232}=4.948\times 10^{-11}\text{ yr}^{-1}$ . Measurement errors ( $2\sigma$ ) range from 0.1% to 0.5% and do not include uncertainties in  $\lambda_{238}$  (0.07%) or  $\lambda_{232}$  (0.5%).

(4) Th isotopic compositions measured by: (A) SIMS at WHOI using the Cameca IMS1270 [63], and (B) PIMMS at Finnigan MAT in Bremen and WHOI using the ThermoFinnigan Neptune; activity ratios calculated using  $\lambda_{230}=9.158\times 10^{-6}\text{ yr}^{-1}$  and  $\lambda_{232}=4.948\times 10^{-11}\text{ yr}^{-1}$ . Measurement errors ( $2\sigma$ ) including uncertainties in the tail correction for PIMMS range from 0.4% to 1% for both techniques and do not include uncertainties in  $\lambda_{230}$  (0.3%) or  $\lambda_{232}$  (0.5%). Reproducibility for the Samoan and Erebus samples as indicated by  $2\sigma$  standard deviation on the average ranges from 0.2% to 1.1%. For the IMS 1270, replicate measurements of rock standards TML and ATHO are reported in Layne and Sims [63]. For the ThermoFinnigan NEPTUNE, during this study, replicate measurements for ATHO ( $n=5$ ) and TML ( $n=5$ ) yield a of ( $^{230}\text{Th}/^{232}\text{Th}$ ) of  $1.015\pm 0.003$  and  $1.074\pm 0.008$ , respectively.

(5) ( $^{234}\text{U}/^{238}\text{U}$ ) measured by PIMMS at WHOI.  $\lambda_{234}=2.823\times 10^{-6}\text{ yr}^{-1}$ , errors ( $2\sigma$ )  $<0.5\%$ ; for these samples ( $^{234}\text{U}/^{238}\text{U}$ )=1 within error, using an equilibrium  $^{234}\text{U}/^{238}\text{U}$  of 54.88 ppm and do not include uncertainties in  $\lambda_{234}$  (0.2%) and  $\lambda_{238}$  (0.07%). NBS 960 was run between each sample to determine mass bias and SEM/Faraday gain. Replicate measurements for ATHO ( $n=3$ ) and TML ( $n=4$ ) during these measurements yield ( $^{234}\text{U}/^{238}\text{U}$ ) =  $1.003\pm 0.004$  and  $1.002\pm 0.004$ , respectively.

component (low  $^{230}\text{Th}/^{232}\text{Th}$  ratios) is greater than the Th/Sr ratio in the depleted component, consistent with the relative compatibilities of Sr and Th.  $^{238}\text{U}/^{232}\text{Th}$  is also correlated with  $^{87}\text{Sr}/^{86}\text{Sr}$ . The Samoan samples' low ( $^{238}\text{U}/^{232}\text{Th}$ ) similarly extend the correlation of ( $^{238}\text{U}/^{232}\text{Th}$ ) with  $^{87}\text{Sr}/^{86}\text{Sr}$  and also change its form from linear to hyperbolic (Fig. 6B). It is not surprising that both  $^{230}\text{Th}/^{232}\text{Th}$  and  $^{238}\text{U}/^{232}\text{Th}$  are correlated with  $^{87}\text{Sr}/^{86}\text{Sr}$ , given that for the entire oceanic basalt suite the variability of  $^{230}\text{Th}/^{238}\text{U}$  ( $\sim 40\%$ ) is much smaller than the range of  $^{230}\text{Th}/^{232}\text{Th}$  and  $^{238}\text{U}/^{232}\text{Th}$  ( $\sim 300\%$ ).

Two end-member processes have been proposed to account for the U–Th disequilibria measured in oceanic

basalts: (1) net elemental fractionation of Th from U at low melt fractions and (2)  $^{230}\text{Th}$  in-growth over the timescale of melt generation. If net elemental fractionation of Th/U during partial melting is the dominant effect, then the U/Th of the mantle source is best determined from the lavas'  $^{230}\text{Th}/^{232}\text{Th}$  activity ratio and  $^{230}\text{Th}/^{232}\text{Th}$  should be better correlated with  $^{87}\text{Sr}/^{86}\text{Sr}$ . On the other hand, if  $^{230}\text{Th}$  in-growth is the fundamental mechanism of U–Th disequilibria, then the U/Th source ratio is best determined from the lavas'  $^{238}\text{U}/^{232}\text{Th}$  activity ratio and  $^{238}\text{U}/^{232}\text{Th}$  should be better correlated with  $^{87}\text{Sr}/^{86}\text{Sr}$ . Previous estimates of correlations between  $^{238}\text{U}/^{232}\text{Th}$  and  $^{230}\text{Th}/^{232}\text{Th}$  vs.

$^{87}\text{Sr}/^{86}\text{Sr}$  for the global oceanic basalt database indicated, based upon linear regression methods, that ( $^{230}\text{Th}/^{232}\text{Th}$ ) was better correlated with  $^{87}\text{Sr}/^{86}\text{Sr}$  [7]. However, these investigations were restricted by limited data sets and assumed a linear functional form, which we show to be incorrect.

To assess the fit of the global oceanic basalt database to a two-component mixing model, we employ a recently developed non-linear inversion method for fitting mixing hyperbolas to ratio–ratio data [40]. We invert both the global database and suite averages to obtain estimates for the five general mixing parameters (two end-member  $x$ - and  $y$ -axis ratio values and the ratio of concentration ratios, which establishes the mixing curvature) and their uncertainties (using both bootstrap and jackknife methods). The results for both inversions are given in Table 3 and shown in Figs. 2 and 3. Also shown in Fig. 3 for comparison is our “best-estimate” two-component mixing model optimized to go through MORB and Samoa data.

Our statistical analysis demonstrates that the binary mixing model accounts for 82% of the variance in the  $^{230}\text{Th}/^{232}\text{Th}$  vs.  $^{87}\text{Sr}/^{86}\text{Sr}$  data and 70% of the variance in the  $^{238}\text{U}/^{232}\text{Th}$  vs.  $^{87}\text{Sr}/^{86}\text{Sr}$  data. We use the  $F$ -statistic to test against the null hypothesis of random variation and find that both datasets test positive against the null hypothesis at the >99% confidence level, arguing that binary mixing is an important source of variation in the samples. The goodness-of-fit statistics (i.e., RMS) indicate that the ( $^{230}\text{Th}/^{232}\text{Th}$ ) vs.  $^{87}\text{Sr}/^{86}\text{Sr}$  data (RMS=0.18) fit a binary mixing model better than ( $^{238}\text{U}/^{232}\text{Th}$ ) vs.  $^{87}\text{Sr}/^{86}\text{Sr}$  (RMS=0.30) (Table 3), which, as described above, has implications for the melting process. Such inferences, however, are subject to the large uncertainties introduced by assuming: (1) that our limited database adequately characterizes the true variability of the unknown global distribution and (2) the model misfit is not significantly influenced by variations due to mixing with additional mantle components (e.g., EM1, HIMU). It is also relevant to note that we have not evaluated the significance in the difference in goodness-of-fit between the ( $^{230}\text{Th}/^{232}\text{Th}$ ) and ( $^{238}\text{U}/^{232}\text{Th}$ ) vs.  $^{87}\text{Sr}/^{86}\text{Sr}$  data to a binary mixing model (e.g., RMS=0.18 vs. 0.30) as this would involve hypothesis testing for non-nested models that is beyond the scope of this paper. Finally, our two different treatments of the data (global database and suite averages) also demonstrate that sampling bias is a concern for the inversion; for the current database, the much larger number of Azores, EPR and

Hawaiian samples are influencing the results of the global database inversion, particularly for ( $^{238}\text{U}/^{232}\text{Th}$ ) vs.  $^{87}\text{Sr}/^{86}\text{Sr}$ .

While our analysis shows that simple two-component mixing of DMM and EM2 explains about 75% of the variation in ( $^{230}\text{Th}/^{232}\text{Th}$ ) and ( $^{238}\text{U}/^{232}\text{Th}$ ) with respect to  $^{87}\text{Sr}/^{86}\text{Sr}$  for the global oceanic database, both data sets also show considerable scatter about their best-fit mixing trends (Fig. 2) that are not explained by binary mixing. This scatter is not surprising given that: (1) the mantle is known to contain at least four distinct components [12,13]; (2) the half-life of  $^{230}\text{Th}$  is short compared to the timescales of mantle upwelling and magma genesis, so processes such as  $^{230}\text{Th}$  in-growth and progressive source depletion are likely to have a significant effect on the lavas'  $^{230}\text{Th}/^{232}\text{Th}$ , particularly for MORB where solid mantle upwelling rates are low [19,41, 42]; and (3) U/Th is likely to be fractionated by melting processes [5,6,10,11,43]. In subsequent sections we discuss the impact of additional source components and petrogenetic processes on the lavas' ( $^{230}\text{Th}/^{232}\text{Th}$ ), ( $^{238}\text{U}/^{232}\text{Th}$ ) and  $^{87}\text{Sr}/^{86}\text{Sr}$ . For many of the OIB suites, like the Azores and Mt. Erebus, mixing with a distinct HIMU mantle component (as shown by the Pb isotopic data) is likely causing these samples to deviate from the simple two-component mixing trends. For most MORB (and some OIB, like Hawaii), the large range and extent of  $^{230}\text{Th}/^{238}\text{U}$  over a limited range of  $^{87}\text{Sr}/^{86}\text{Sr}$  indicates that melt generation and magma transport processes are significantly influencing both  $^{230}\text{Th}/^{232}\text{Th}$  and  $^{238}\text{U}/^{232}\text{Th}$ .

### 2.3. Correlations of ( $^{230}\text{Th}/^{232}\text{Th}$ ) and ( $^{238}\text{U}/^{232}\text{Th}$ ) with $^{143}\text{Nd}/^{144}\text{Nd}$ : two-component mixing?

As with  $^{87}\text{Sr}/^{86}\text{Sr}$ , for the current global oceanic basalt database, correlations between ( $^{230}\text{Th}/^{232}\text{Th}$ ) and ( $^{238}\text{U}/^{232}\text{Th}$ ) versus  $^{143}\text{Nd}/^{144}\text{Nd}$  (expressed as  $\epsilon_{\text{Nd}}$ ) are approximated by simple two-component mixing (Fig. 4). The Samoan samples' low ( $^{230}\text{Th}/^{232}\text{Th}$ ), ( $^{238}\text{U}/^{232}\text{Th}$ ) and  $^{143}\text{Nd}/^{144}\text{Nd}$  greatly extend these global correlations and also change their form from linear to hyperbolic. The positive slopes of these trends are consistent with the MORB and OIB Th–Sr and Sr–Nd isotope correlations and support the idea that the depleted mantle is, at least in part, complementary to the more enriched continental crust. When the hyperbolic trend is interpreted as reflecting a mixing line, its curvature indicates that the Th/Nd ratio in the enriched component (low  $^{230}\text{Th}/^{232}\text{Th}$  ratios) is greater than the Th/Nd ratio in the depleted

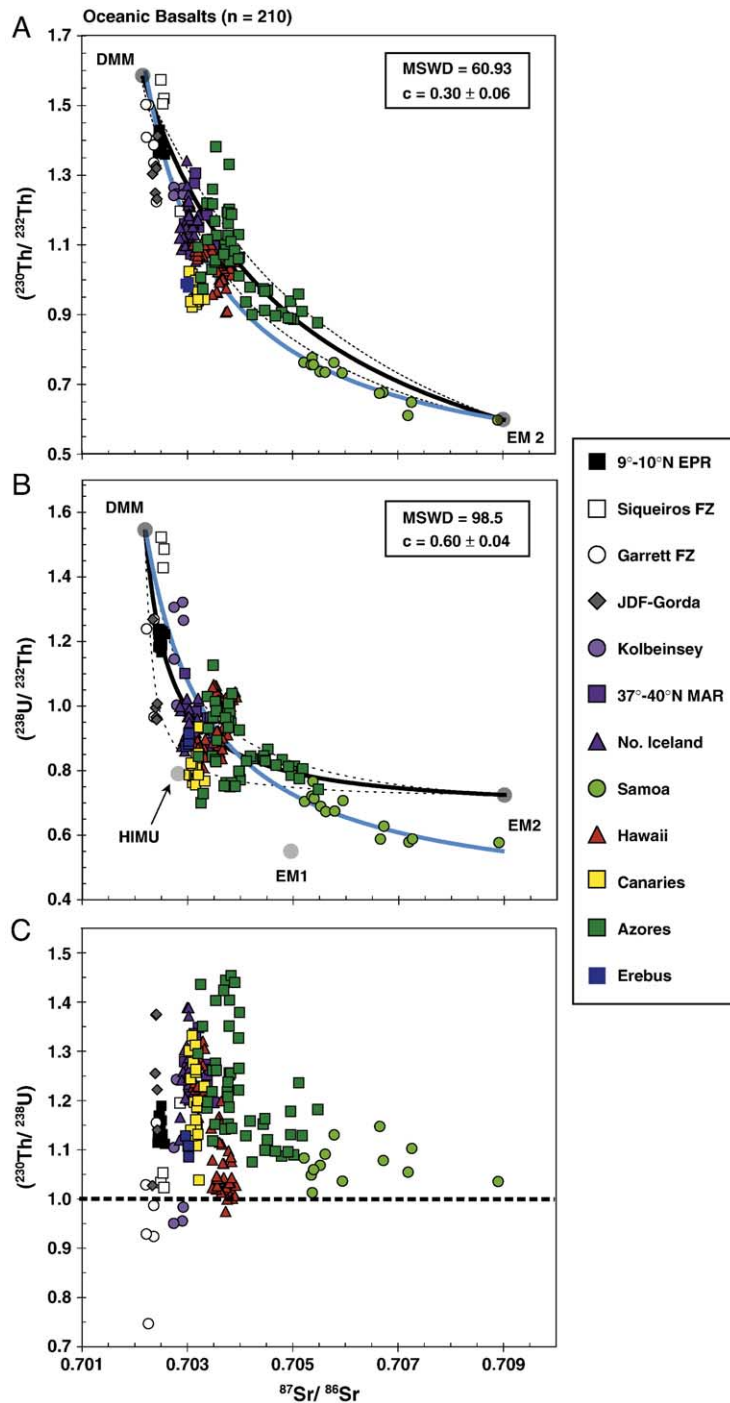


Fig. 2.  $(^{230}\text{Th}/^{232}\text{Th})$ ,  $(^{238}\text{U}/^{232}\text{Th})$  and  $(^{230}\text{Th}/^{238}\text{U})$  versus  $^{87}\text{Sr}/^{86}\text{Sr}$  for mid-ocean ridge and ocean island basalts measured by mass spectrometric methods (see Fig. 1 for references). Blue line represents our “best-estimate” two-component mixing model optimized to go through MORB and Samoa data. Black lines represents inverted best-fit two component mixing model (solid) and 95% confidence intervals (dashed) for the estimated hyperbolic curvature. 95% confidence intervals are calculated from the standard errors. For the DMM and EM2 end-members, both  $(^{230}\text{Th}/^{232}\text{Th})$  and  $(^{238}\text{U}/^{232}\text{Th})$  are well defined by the EPR and Samoan data arrays. For the EM1 and HIMU endmembers there are no  $^{230}\text{Th}/^{232}\text{Th}$  data; however, literature data for Pitcairn (EM1 endmember), and Mangai-Tubai (HIMU end-member) define the location of these end member mantle components for  $(^{238}\text{U}/^{232}\text{Th})$ . Note that both HIMU and EM1 are located slightly below the best-fit mixing curve for DMM–EM2 [58–60].

Table 3

Prior conditions and posterior results using a non-linear, maximum likelihood methods for inverting ratio–ratio data [40,64]

	DMM						EM2						Concentration ratio			Goodness Fit Statistics	
	<i>x</i>	SE ( <i>x</i> )BS	SE ( <i>x</i> )JK	<i>y</i>	SE ( <i>y</i> )BS	SE ( <i>y</i> )JK	<i>x</i>	SE ( <i>x</i> )BS	SE ( <i>x</i> )JK	<i>y</i>	SE ( <i>y</i> )BS	SE ( <i>y</i> )JK	<i>c</i>	SE ( <i>c</i> )BS	SE ( <i>c</i> )JK	MSWD	RMS
( <sup>230</sup> Th/ <sup>232</sup> Th) vs. <sup>87</sup> Sr/ <sup>86</sup> Sr prior	0.7022			1.60			0.709			0.60			0.15			73.40	
Whole data set ( <i>n</i> =210)	0.7021	5E-06	4E-06	1.59	0.02	0.02	0.709	8E-07	8E-07	0.60	0.05	0.02	0.30	0.03	0.03	60.93	0.18
Averages ( <i>n</i> =12)	0.7021	2E-05	2E-05	1.55	0.02	0.02	0.709	8E-07	6E-05	0.60	0.006	0.006	0.24	0.03	0.03		0.19
( <sup>238</sup> U/ <sup>232</sup> Th) vs. <sup>87</sup> Sr/ <sup>86</sup> Sr priors	0.7022			1.55			0.709			0.55			0.15			112.42	
Whole data set ( <i>n</i> =209)	0.7022	6E-05	5E-05	1.55	0.03	0.03	0.709	2E-07	2E-07	0.72	0.04	0.04	0.06	0.02	0.02	98.50	0.30
Averages ( <i>n</i> =12)	0.7022	2E-04	6E-05	1.53	0.02	0.02	0.709	4E-07	3E-07	0.59	0.02	0.01	0.10	0.02	0.02		0.39
( <sup>230</sup> Th/ <sup>232</sup> Th) vs. εNd priors	10.8			1.60			-2.9			0.60			0.33			44.15	
Whole data set ( <i>n</i> =161)	12.51	0.49	0.49	1.56	0.01	0.01	-3.07	0.59	0.59	0.60	0.02	0.02	0.61	0.06	0.06	37.74	0.13
Averages ( <i>n</i> =10)	12.61	0.47	0.44	1.58	0.01	0.01	-3.04	0.56	0.57	0.61	0.01	0.01	0.60	0.04	0.04		0.17
( <sup>238</sup> U/ <sup>232</sup> Th) vs. εNd priors	10.8			1.55			-2.9			0.55			0.40				
Whole data set ( <i>n</i> =161)	12.53	0.47	0.47	1.52	0.01	0.01	-3.38	0.53	0.53	0.64	0.04	0.03	0.29	0.04	0.04	56.98	0.21
Averages ( <i>n</i> =10)	13.55	0.44	0.47	1.51	0.01	0.03	-3.43	0.57	0.62	0.59	0.02	0.02	0.47	0.09	0.12		0.19

(1) Prior values for the model parameters are required to condition the inversion to calculate the five general mixing parameters (*X*s, *Y*s in DMM and EM2 and the ratio of the concentration ratios for the two components). The end-member isotope ratio estimates (unlike the concentration ratio estimate) are sensitive to the initial values used in the inversion. This results from the fact that the data fit the model equally well for any set of end-members on the mixing hyperbola, which in principle can extend to arbitrarily large values outside the range of the data [40].

(2) For this inversion uncertainties in the data are assumed to be analytical and uniform (1% for <sup>230</sup>Th/<sup>232</sup>Th and <sup>238</sup>U/<sup>232</sup>Th, 10 ppm for <sup>87</sup>Sr/<sup>86</sup>Sr, and 0.1 epsilon units for ε<sub>Nd</sub>).

(3) Posterior uncertainties on fit parameters represent standard errors (S.E.) calculated using both bootstrapping (BS), and jackknife (JK) methods, see [40,64] for details.

(4) MSWD (mean square of weighted deviates) represents the misfit between the two-component mixing model and the data.

(5) RMS (residual mean square) is defined as the residual sum of squares (RSS) divided by the degrees of freedom (DOF), which for binary mixing, the DOF is the number data points minus the number model parameters, or *N*–5; thus RMS=RSS/(*N*–5). Conceptually this is the variance of the residuals from the model. Because this model [40] normalizes the data variance to one prior to inversion, the variance explained by the model, or “sum of squares due to regression” (SSreg)=1-rms.

(6) Inversion of the <sup>238</sup>U/<sup>232</sup>Th data suites did not include Garrett sample with high U/Th.

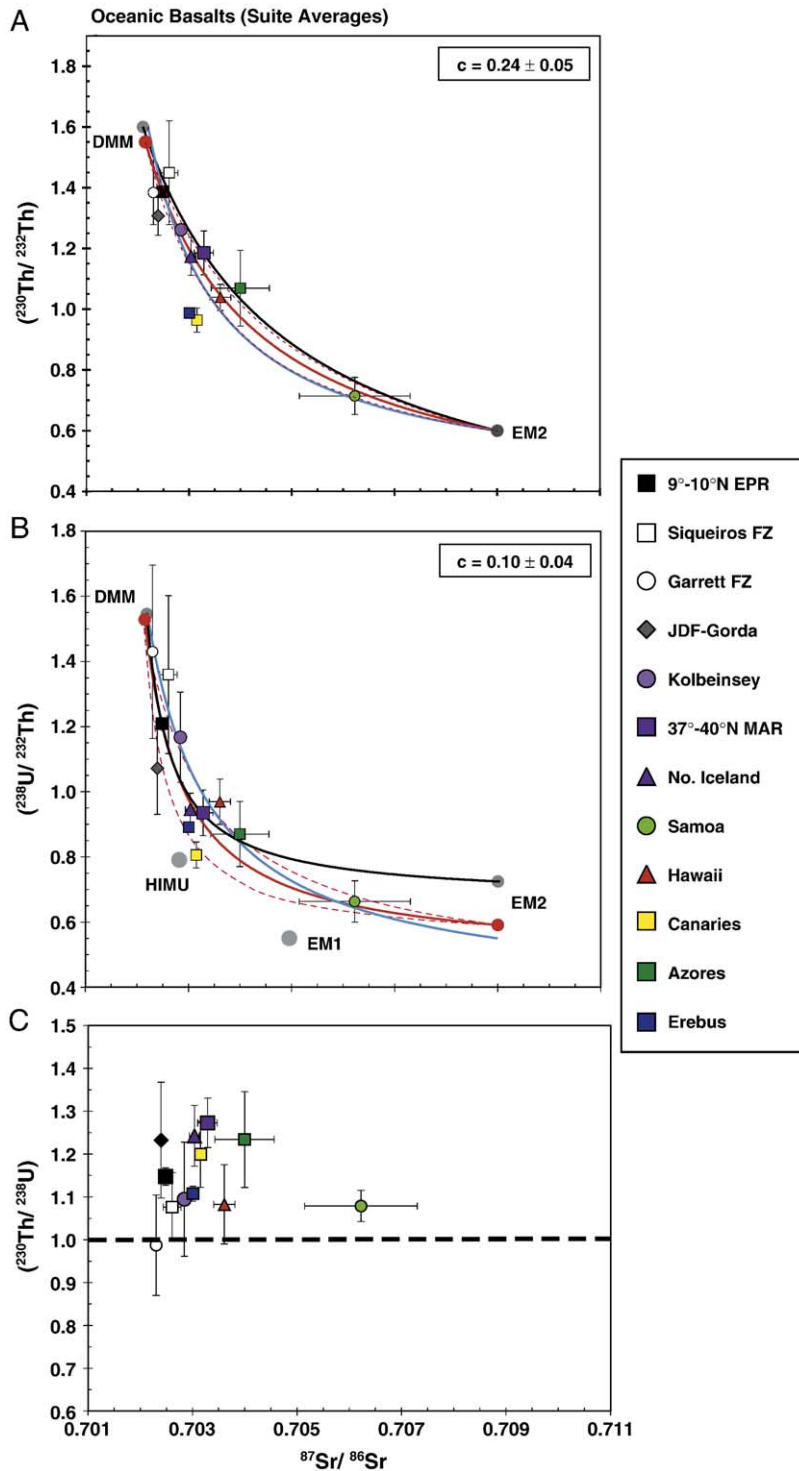


Fig. 3. Suite averages for  $(^{230}\text{Th}/^{232}\text{Th})$ ,  $(^{238}\text{U}/^{232}\text{Th})$  and  $(^{230}\text{Th}/^{238}\text{U})$  and  $^{87}\text{Sr}/^{86}\text{Sr}$  for the mid-ocean ridge and ocean island basalts shown in preceding figure. Error bars represent 1-sigma standard deviation about the mean. Blue line represents our “best-estimate” two-component mixing model optimized to go through MORB and Samoa data; solid black line represents inverted best-fit two-component mixing model for global data suite as in Fig. 6; red lines represent the inverted best-fit two-component mixing trend and 95% confidence intervals (dashed) on the estimated hyperbolic curvature for the suite averages.

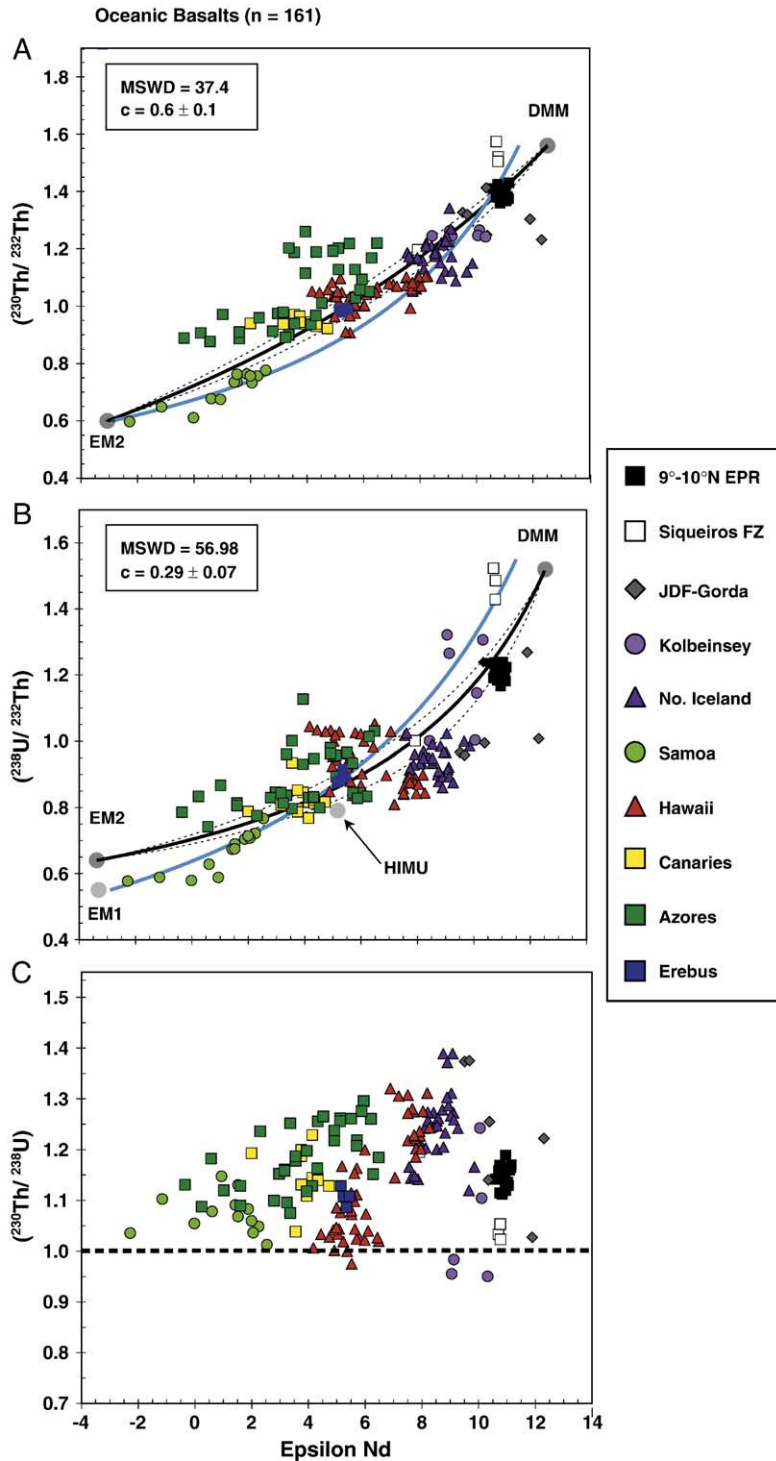


Fig. 4.  $(^{230}\text{Th}/^{232}\text{Th})$ ,  $(^{238}\text{U}/^{232}\text{Th})$  and  $(^{230}\text{Th}/^{238}\text{U})$  versus Epsilon Nd for mid-ocean ridge and ocean island basalts measured by mass spectrometric methods (see Fig. 5 for references). Blue line represents our “best-estimate” two-component mixing model optimized to go through MORB and Samoa data. Black lines represents inverted best-fit two component mixing model (solid) and 95% confidence intervals (dashed) for the estimated hyperbolic curvature. 95% confidence intervals are calculated from the standard errors. End-member mantle components for EMII and DMM are from this study; for EMI and HIMU,  $^{238}\text{U}/^{232}\text{Th}$  and  $^{143}\text{Nd}/^{144}\text{Nd}$  come from literature [58–60]. Note that both HIMU and EM1 are located, within uncertainties, along the best-fit mixing curve for DMM–EM2.

component, consistent with the relative compatibilities of Nd and Th.

To assess the fit of the global oceanic basalt database to a two-component mixing model we again apply the non-linear, maximum likelihood method to invert the  $^{238}\text{U}/^{232}\text{Th}$  and  $^{230}\text{Th}/^{232}\text{Th}$  vs.  $^{143}\text{Nd}/^{144}\text{Nd}$  data for concentration ratios (hyperbolic curvature) and end-member isotopic components [40]. This analysis (Table 3 and Figs. 4 and 5) demonstrates that: (1) binary mixing model accounts for 87% of the variance in the  $(^{230}\text{Th}/^{232}\text{Th})$  vs.  $\epsilon_{\text{Nd}}$  and 79% of the variance in the  $(^{238}\text{U}/^{232}\text{Th})$  vs.  $\epsilon_{\text{Nd}}$ ; (2) the goodness-of-fit statistics (i.e., RMS) indicate that  $(^{230}\text{Th}/^{232}\text{Th})$  vs.  $\epsilon_{\text{Nd}}$  data (RMS=0.13) fit a binary mixing model better than  $(^{238}\text{U}/^{232}\text{Th})$  vs.  $\epsilon_{\text{Nd}}$  (RMS=0.21); and (3) sampling bias influences the inversion results (Fig. 5).

Like  $^{87}\text{Sr}/^{86}\text{Sr}$ , it is also important to note that the global correlations of  $^{143}\text{Nd}/^{144}\text{Nd}$  with  $(^{230}\text{Th}/^{232}\text{Th})$  and  $(^{238}\text{U}/^{232}\text{Th})$  are based upon limited data sets and are only approximated by simple two-component mixing of DMM and EM2, as these data also show considerable scatter about the inverted best-fit mixing trends. This scatter is again attributed to both mixing of additional mantle source components (e.g. EM1 and HIMU) and the effect of melting processes on both  $(^{230}\text{Th}/^{232}\text{Th})$  and  $(^{238}\text{U}/^{232}\text{Th})$ .

#### 2.4. U–Th systematics and Pb isotopes: influence of additional source components

The Pb isotopic data show a more complex relationship with  $(^{230}\text{Th}/^{232}\text{Th})$  and  $(^{238}\text{U}/^{232}\text{Th})$  (Fig. 6). On plots of  $(^{230}\text{Th}/^{232}\text{Th})$ – $^{206}\text{Pb}/^{204}\text{Pb}$  and  $(^{238}\text{U}/^{232}\text{Th})$ – $^{206}\text{Pb}/^{204}\text{Pb}$ , the oceanic data form four arrays, which are somewhat analogous to the patterns observed for  $^{87}\text{Sr}/^{86}\text{Sr}$ – $^{206}\text{Pb}/^{204}\text{Pb}$  (and  $^{143}\text{Nd}/^{144}\text{Nd}$ – $^{206}\text{Pb}/^{204}\text{Pb}$ ). When interpreted in terms of mixing, these arrays require four mantle-source components corresponding to the end-members DMM, HIMU, EM1 and EM2 that define the mantle tetrahedron [12,13].

Based upon these multiple Pb isotopic arrays (Fig. 6) and  $(^{238}\text{U}/^{232}\text{Th})$  literature data for Pitcairn (EM1 end-member) and Mangai-Tubai (HIMU end-member), we infer for some sample suites that their deviation from the two-component Th–Sr array reflects mixing with additional components beyond DMM and EM2 (Fig. 3). For example, the Mt. Erebus samples and some of the Azores samples lie markedly below the DMM and EM2 Th–Sr mixing trends and have high  $^{206}\text{Pb}/^{204}\text{Pb}$ , low  $^{87}\text{Sr}/^{86}\text{Sr}$  and intermediate  $^{238}\text{U}/^{232}\text{Th}$ , forming

arrays that project toward the inferred HIMU end-member. The Canaries samples also lie significantly below the global Th–Sr tend; however these particular samples do not have Pb isotopic characteristics requiring a HIMU or EM1 component in their source (Fig. 6), suggesting that their displacement from the Th–Sr array is either a manifestation of recent processes perturbing the U–Th isotopic systematics (magmatic, metasomatic, and/or secondary) or mixing with an additional unidentified source component. For the Th–Nd correlations, it is interesting to note that the inferred HIMU and EM1 end-member components lie almost directly on the inverted two-component mixing trend and that this inferred HIMU end-member is nearly coincident with the Mt. Erebus samples (Fig. 4).

$(^{230}\text{Th}/^{232}\text{Th})$ ,  $(^{238}\text{U}/^{232}\text{Th})$  and  $^{208}\text{Pb}/^{206}\text{Pb}$  have all been used, with various assumptions and caveats, as proxies for the  $^{232}\text{Th}/^{238}\text{U}$  of the lavas' mantle source. These different proxies yield discrepant results with estimates of Th/U from  $^{208}\text{Pb}/^{206}\text{Pb}$  typically being much higher than values inferred from  $(^{230}\text{Th}/^{232}\text{Th})$  and  $(^{238}\text{U}/^{232}\text{Th})$ . The origin of this discrepancy, referred to as the “kappa conundrum”, has long been debated [44–46]. The observation that, for the current global oceanic database, both  $(^{230}\text{Th}/^{232}\text{Th})$  and  $(^{238}\text{U}/^{232}\text{Th})$  behave more coherently with  $^{87}\text{Sr}/^{86}\text{Sr}$  and  $^{143}\text{Nd}/^{144}\text{Nd}$  than do the Pb isotopes (including  $^{208}\text{Pb}/^{206}\text{Pb}$ ) suggests that the U–Th–Pb isotopic system is “decoupled” from the other isotopic systems (e.g. Rb/Sr, Sm/Nd, U/Th), and both  $(^{230}\text{Th}/^{232}\text{Th})$  and  $(^{238}\text{U}/^{232}\text{Th})$  are better proxies for the lavas' Th/U source ratio. This is not necessarily surprising given that U, Th, Rb, Sr, Sm, Nd are predominantly lithophile in their character/behavior, whereas Pb is also highly siderophile and chalcophile (see e.g. [47]). From this perspective, it is likely that U/Pb and Th/Pb have been fractionated by processes (e.g. core formation, etc.) and phases (sulfides) not influencing lithophile parent–daughter systems.

#### 2.5. Influence of magma genesis on observed trends

Most MORB (and some OIB, like Hawaii) show a large range and extent of  $(^{230}\text{Th}/^{238}\text{U})$  over a limited range of Nd, Sr and Pb isotopes (Figs. 2–6). This large range and extent of  $(^{230}\text{Th}/^{238}\text{U})$  disequilibria suggests that melting processes significantly influence the lavas'  $(^{230}\text{Th}/^{232}\text{Th})$  and  $(^{238}\text{U}/^{232}\text{Th})$ . However, because of the hyperbolic nature of the inverted mixing trends (Fig. 2), it is difficult to deconvolve the influence of simple two-component mixing from the effects of melting, particularly for MORB [9].

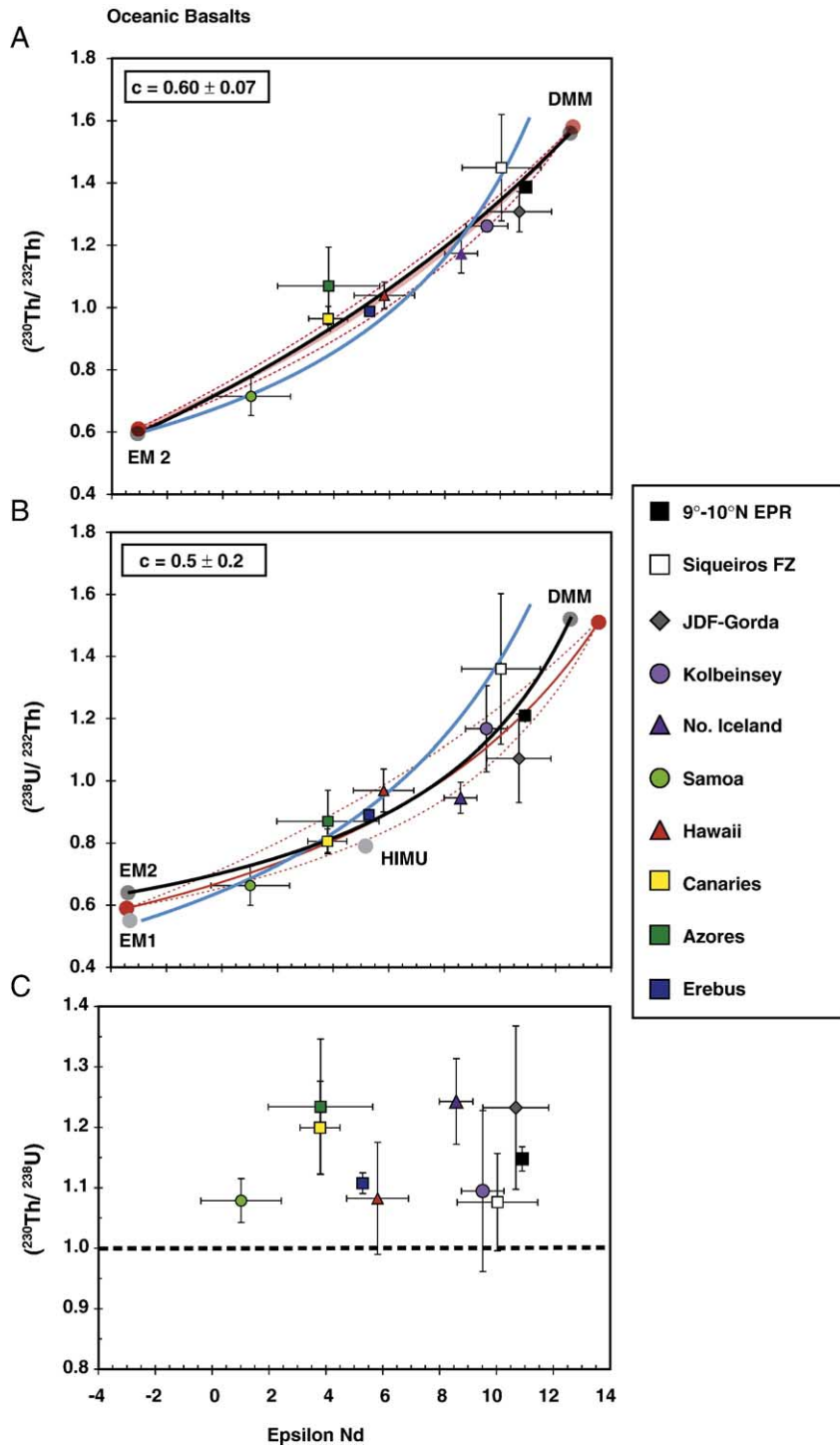


Fig. 5. Suite averages for  $(^{230}\text{Th}/^{232}\text{Th})$ ,  $(^{238}\text{U}/^{232}\text{Th})$  and  $(^{230}\text{Th}/^{238}\text{U})$  and Epsilon Nd for the mid-ocean ridge and ocean island basalts shown in preceding figure. Error bars represent 1-sigma standard deviation about the mean. Blue line represents our “best-estimate” two-component mixing model optimized to go through MORB and Samoa data; solid black lines represents inverted best fit two component mixing model for global data suite as in Fig. 8; red lines represents the inverted best-fit two-component mixing trend (solid) and 95% confidence intervals (dashed) on the estimated hyperbolic curvature for the suite averages. The large differences in the inverted concentration ratio and end-member isotopic components for the global data base vs. suite average inversions (Fig. 4) indicate that the much larger number of Azores, EPR and Hawaiian samples are influencing the results of the global data base inversion, particularly for  $^{238}\text{U}/^{232}\text{Th}$  vs.  $\epsilon_{\text{Nd}}$ .

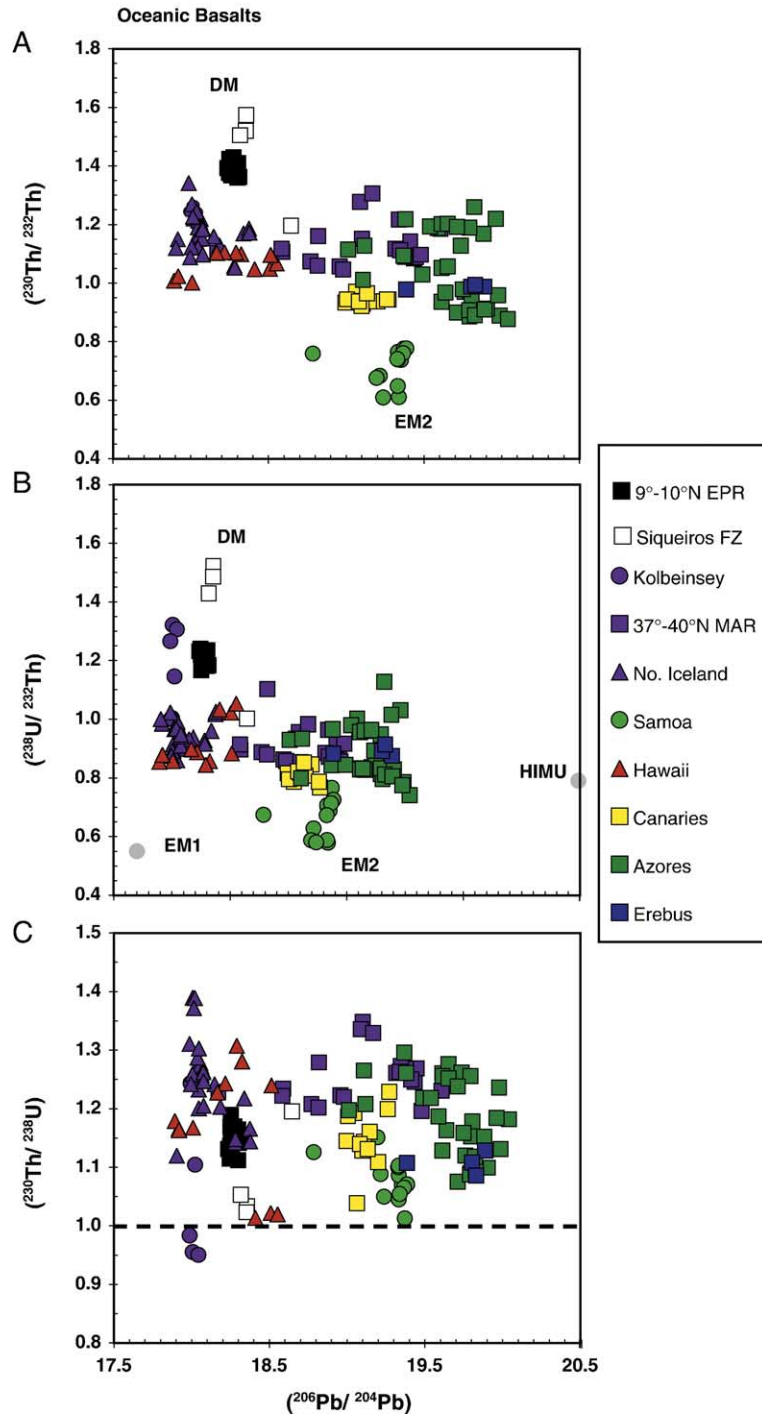


Fig. 6.  $(^{230}\text{Th}/^{232}\text{Th})$ ,  $(^{238}\text{U}/^{232}\text{Th})$  and  $(^{230}\text{Th}/^{238}\text{U})$  versus  $^{206}\text{Pb}/^{204}\text{Pb}$  for mid-ocean ridge and ocean island basalts measured by mass spectrometry (see Fig. 1 for data references). End-member mantle components for EMII and DMM are from this study; for EMI and HIMU,  $^{238}\text{U}/^{232}\text{Th}$  and  $^{206}\text{Pb}/^{204}\text{Pb}$  come from literature [58–60]. The four endmembers define four distinct components.

In an attempt to assess the extent to which our best-fit two-component mixing models are consistent with MORB's large range of  $(^{230}\text{Th}/^{232}\text{Th})$  and  $(^{238}\text{U}/$

$^{232}\text{Th})$  over a very limited range of  $^{87}\text{Sr}/^{86}\text{Sr}$  (Fig. 2), we represent the data in a form (Fig. 7A) that enables us to compare the slope  $[\Delta(^{230}\text{Th}/^{232}\text{Th})/\Delta(^{87}\text{Sr}/^{86}\text{Sr})]$  of

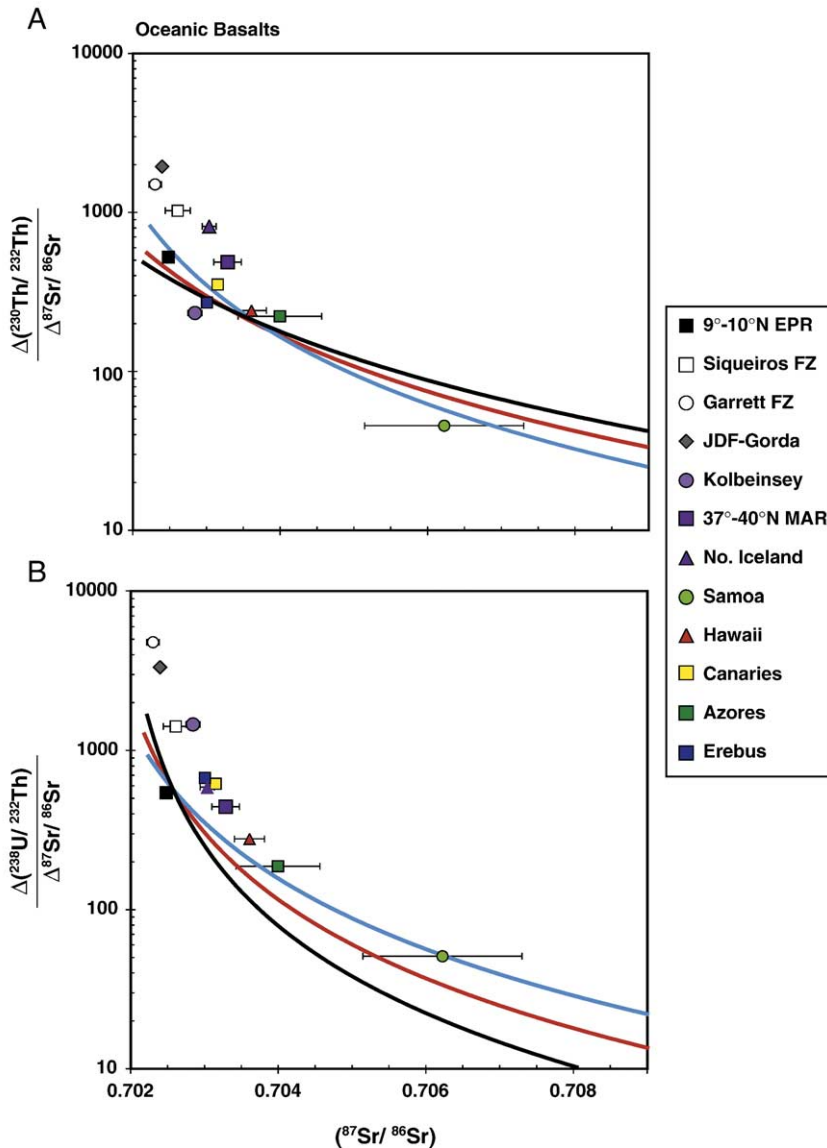


Fig. 7. (A)  $\Delta(^{230}\text{Th}/^{232}\text{Th})/\Delta(^{87}\text{Sr}/^{86}\text{Sr})$ ; (B)  $\Delta(^{238}\text{U}/^{232}\text{Th})/\Delta(^{87}\text{Sr}/^{86}\text{Sr})$  versus average  $^{87}\text{Sr}/^{86}\text{Sr}$  for the individual MORB and OIB data sets. Error bars on  $^{87}\text{Sr}/^{86}\text{Sr}$  represent 1-sigma standard deviation about the average.  $\Delta(^{230}\text{Th}/^{232}\text{Th})/\Delta(^{87}\text{Sr}/^{86}\text{Sr})$  is the estimated slope of the individual suites in plots of  $^{230}\text{Th}/^{232}\text{Th}$  versus  $^{87}\text{Sr}/^{86}\text{Sr}$ , and is defined as the range (maximum–minimum) of  $^{230}\text{Th}/^{232}\text{Th}$  divided by the range (maximum–minimum) of  $^{87}\text{Sr}/^{86}\text{Sr}$  for the individual suites.  $\Delta(^{238}\text{U}/^{232}\text{Th})/\Delta(^{87}\text{Sr}/^{86}\text{Sr})$  is defined similarly. Also shown are the calculated derivatives of the hyperbolic mixing curves for the 3 two-component mixing models given in Figs. 2 and 3 (“best-guess”=blue line, “best-fit global trend”=black line, “best-fit suite averages”=red line).

each data suite (e.g. 9–10°N EPR, Hawaii, Azores, etc.) to the derivatives of the calculated hyperbolic mixing curves for each of the three two-component mixing models at a given value of  $^{87}\text{Sr}/^{86}\text{Sr}$ . At low  $^{87}\text{Sr}/^{86}\text{Sr}$  the mixing hyperbole are steep [i.e. large  $\Delta(^{230}\text{Th}/^{232}\text{Th})/\Delta(^{87}\text{Sr}/^{86}\text{Sr})$ ], whereas at high  $^{87}\text{Sr}/^{86}\text{Sr}$  the slopes of the mixing curves are shallower [i.e. small  $\Delta(^{230}\text{Th}/^{232}\text{Th})/\Delta(^{87}\text{Sr}/^{86}\text{Sr})$ ]. Fig. 7B is a similar representation for  $\Delta(^{238}\text{U}/^{232}\text{Th})/\Delta(^{87}\text{Sr}/^{86}\text{Sr})$

versus average ( $^{87}\text{Sr}/^{86}\text{Sr}$ ). In these representations (Fig. 7A and B) the closeness of a sample suite’s estimated slope to the mixing curve implies the degree to which the data is explained by two-component mixing; a sample suite which lies on the mixing curve can, in principle, be explained entirely by two-component mixing, whereas a sample suite’s deviation from the mixing curve implies other processes or additional sources are also involved.

For most MORB and OIB suites, the variation of ( $^{230}\text{Th}/^{232}\text{Th}$ ) and ( $^{238}\text{U}/^{232}\text{Th}$ ) is greater than would be predicted by both our “best-estimate” and “best-fit” twocomponent mixing models. While this observation does not rule out mixing with an additional, unaccounted source component (e.g. a component with low  $^{230}\text{Th}/^{232}\text{Th}$ ,  $^{238}\text{U}/^{232}\text{Th}$  and  $^{87}\text{Sr}/^{86}\text{Sr}$ ), it is consistent with other observations and models indicating that melting processes are affecting the lavas’ ( $^{230}\text{Th}/^{232}\text{Th}$ ) and ( $^{238}\text{U}/^{232}\text{Th}$ ). The observation that, for most MORB and many OIB suites, both the range of ( $^{230}\text{Th}/^{232}\text{Th}$ ) and ( $^{238}\text{U}/^{232}\text{Th}$ ) are greater than the variation predicted by the simple two-component mixing models suggests that both  $^{230}\text{Th}$  ingrowth (over the timescale of magma genesis) and net elemental U/Th fractionation (at low melt fractions and porosities) are contributing to the observed ( $^{230}\text{Th}/^{238}\text{U}$ ) disequilibria.

For the MORB and OIB suites there is also an inverse relationship between the relative variability of ( $^{230}\text{Th}/^{238}\text{U}$ ) and  $^{87}\text{Sr}/^{86}\text{Sr}$  [expressed as  $\sigma(^{230}\text{Th}/^{238}\text{U})/\sigma^{87}\text{Sr}/^{86}\text{Sr}$ ] and the degree of source enrichment, as indicated by  $^{87}\text{Sr}/^{86}\text{Sr}$  (Fig. 8). Depleted MORB samples show the largest variability of ( $^{230}\text{Th}/^{238}\text{U}$ ) and very little variation in  $^{87}\text{Sr}/^{86}\text{Sr}$ , whereas the more “enriched” OIB suites show less variability in ( $^{230}\text{Th}/^{238}\text{U}$ ) but a larger range of  $^{87}\text{Sr}/^{86}\text{Sr}$  (Fig. 2). We interpret this inverse relationship in terms of differences in the melting regimes beneath mid-ocean ridges and

ocean islands. Mid-ocean ridges have low solid mantle upwelling rates (which can be inferred from their spreading rates) and they typically do not have a significant lithospheric “lid” truncating their melting column. MORB, as a consequence, represent large average melt fractions derived at low melting rates over a range of porosities and depths. These variable porosities and low melting rates, in combination with changes in the source lithology over the length of the melting column (due to both progressive source depletion and the garnet-spinel phase transition), lead to a large range and extent of ( $^{230}\text{Th}/^{238}\text{U}$ ) for MORB [i.e. large  $\sigma(^{230}\text{Th}/^{238}\text{U})$ ] [11,19,41,48,49]. In contrast, the solid mantle upwelling rates are higher beneath ocean islands [10,50,51], and the length of the melting column and subsequent average degree of melting is strongly controlled by the thickness of the overlying lithosphere. OIB, as a consequence, represent smaller average melt fractions derived at higher melting rates over a more limited range of porosities and depths. OIB’s higher melting rates, shorter melt columns and smaller average melt fractions lead to a smaller range of ( $^{230}\text{Th}/^{238}\text{U}$ ) [i.e. small  $\sigma(^{230}\text{Th}/^{238}\text{U})$ ] [5,8,10]. Differences in the MORB and OIB melting regimes can also explain variations in the degree of source enrichment (i.e.  $\sigma^{87}\text{Sr}/^{86}\text{Sr}$ ). Because this isotopically and trace-element enriched component (either as “eclogitic veins” in the upper mantle, “eclogitic plums” in the plume, or

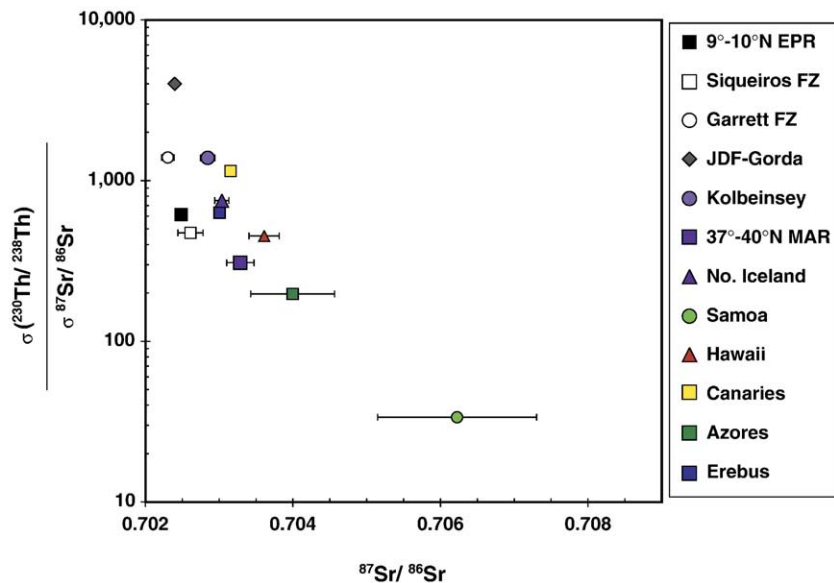


Fig. 8.  $\sigma(^{230}\text{Th}/^{238}\text{U})/\sigma^{87}\text{Sr}/^{86}\text{Sr}$  versus average  $^{87}\text{Sr}/^{86}\text{Sr}$  for the individual MORB and OIB data sets. Error bars on  $^{87}\text{Sr}/^{86}\text{Sr}$  represent 1-sigma standard deviation.  $\sigma(^{230}\text{Th}/^{238}\text{U})/\sigma^{87}\text{Sr}/^{86}\text{Sr}$  is defined as the 1-sigma standard deviation of ( $^{230}\text{Th}/^{238}\text{U}$ ) divided by the 1-sigma standard deviation of  $^{87}\text{Sr}/^{86}\text{Sr}$  for the individual suites.

metasomatized harzburgite) melts preferentially over ambient upper mantle peridotite [52,53], the degree to which enriched compositions are preferentially sampled depends on the overall degree of melting. MORB represent large melt fractions suggesting that melts from depleted peridotite are the dominant magma component, consistent with their low and relatively constant  $^{87}\text{Sr}/^{86}\text{Sr}$  (i.e. small  $\sigma^{87}\text{Sr}/^{86}\text{Sr}$ ). OIB, on the other hand, represent smaller melt fractions and as a result any subordinate “enriched” component is proportionally more significant, consistent with OIBs enriched and variable  $^{87}\text{Sr}/^{86}\text{Sr}$  (i.e. large  $\sigma^{87}\text{Sr}/^{86}\text{Sr}$ ). In this scenario, the variation in OIB is a complex function of lithospheric thickness (and age), potential temperature and melting rate of the upwelling mantle, and the lithology, composition and abundance of the enriched component.

## 2.6. Th/U in DMM, EM2 and BSE

### 2.6.1. DMM

The MORB U-series data show a large range in both ( $^{238}\text{U}/^{232}\text{Th}$ ) and ( $^{230}\text{Th}/^{232}\text{Th}$ ), with the Pacific MORB data typically more depleted than the Atlantic MORB data. Based upon our maximum likelihood regressions for ( $^{238}\text{U}/^{232}\text{Th}$ ) and ( $^{230}\text{Th}/^{232}\text{Th}$ ) versus both  $^{87}\text{Sr}/^{86}\text{Sr}$  and  $^{143}\text{Nd}/^{144}\text{Nd}$  (Table 3) we calculate a range of DMM Th/U from 1.9 to 2.0. This estimate is, within uncertainty, the same as DMM Th/U (1.9 to 1.96) calculated using either the ( $^{230}\text{Th}/^{232}\text{Th}$ ) or ( $^{238}\text{U}/^{232}\text{Th}$ ) of the Siqueiros DMORBs, which have small  $^{230}\text{Th}$  excesses (ca. 1%) and are demonstrably young based upon their large  $^{226}\text{Ra}$  excesses [18]. These estimates are lower, by about 10%, than Th/U of D-DMM estimated by Workman et al. [54].

### 2.6.2. EM2

Based upon our maximum likelihood regressions for ( $^{238}\text{U}/^{232}\text{Th}$ ) and ( $^{230}\text{Th}/^{232}\text{Th}$ ) versus both  $^{87}\text{Sr}/^{86}\text{Sr}$  and  $^{143}\text{Nd}/^{144}\text{Nd}$  (Table 3) we calculate a range of Th/U for EM2 from 5.1 to 5.5. This estimate is essentially the same as the EM2 Th/U (5.1–5.3) calculated using either the ( $^{230}\text{Th}/^{232}\text{Th}$ ) or ( $^{238}\text{U}/^{232}\text{Th}$ ) of the most enriched Samoan sample 78-1, which has a 4%  $^{230}\text{Th}$  excess and is demonstrably young based on its 8%  $^{226}\text{Ra}$  excess. This estimate is about 15% higher than EM2 Th/U of 4.42 estimated by Workman et al. [14].

### 2.6.3. BSE

As advocated by Allègre and Condomines [1], the correlation of Th–Sr has been used to estimate the Th/U

ratio of the bulk silicate Earth (BSE). Using the inverted two-component mixing trends and 95% confidence intervals about these trends (Figs. 2 and 3), and assuming a BSE value for  $^{87}\text{Sr}/^{86}\text{Sr}$  of 0.7045–0.7050, we calculate a Th/U for the BSE of 3.20–3.81 using ( $^{230}\text{Th}/^{232}\text{Th}$ ) vs.  $^{87}\text{Sr}/^{86}\text{Sr}$  and 3.53–4.57 using ( $^{238}\text{U}/^{232}\text{Th}$ ) vs.  $^{87}\text{Sr}/^{86}\text{Sr}$ .

The Th–Nd and U/Th–Nd correlations can also be used to estimate the Th/U ratio of the BSE. In principle, these estimates are better constrained than the estimates from the correlations with Sr isotopes, as our knowledge of the BSE  $^{143}\text{Nd}/^{144}\text{Nd}$  is much better (though recent work by Boyet and Carlson [55] leave open the possibility that CI chondrites are not a good end-member model for the Earth). Using the inverted two-component mixing trends and 95% confidence intervals about these trends (Figs. 4 and 5), and an initial  $\epsilon_{\text{Nd}}$  of 0, we calculate a BSE Th/U of 4.05–4.47 using ( $^{230}\text{Th}/^{232}\text{Th}$ ) vs.  $\epsilon_{\text{Nd}}$  and 4.24–4.77 using ( $^{238}\text{U}/^{232}\text{Th}$ ) vs.  $\epsilon_{\text{Nd}}$ .

Finally, as noted by Allègre et al. [56], a similar approach can be used with ( $^{208}\text{Pb}/^{206}\text{Pb}$ )\* (Fig. 9), where ( $^{208}\text{Pb}/^{206}\text{Pb}$ )\* is defined as:

$$(^{208}\text{Pb}/^{206}\text{Pb})^* = \frac{\frac{^{208}\text{Pb}}{^{204}\text{Pb}} - \left(\frac{^{208}\text{Pb}}{^{204}\text{Pb}}\right)_{\text{CD}}}{\frac{^{206}\text{Pb}}{^{204}\text{Pb}} - \left(\frac{^{206}\text{Pb}}{^{204}\text{Pb}}\right)_{\text{CD}}}$$

This approach assumes that the BSE has evolved as a closed system since 4.55 Ga, and calculates the BSE by evaluating the intersection of the negative trend between ( $^{208}\text{Pb}/^{206}\text{Pb}$ )\* and ( $^{230}\text{Th}/^{232}\text{Th}$ ) {or ( $^{238}\text{U}/^{232}\text{Th}$ )} with the theoretical ( $^{208}\text{Pb}/^{206}\text{Pb}$ )\* ratio calculated for a range of Th/U ratios (Fig. 9). This approach yields an intercept of 0.74–0.78 for ( $^{208}\text{Pb}/^{206}\text{Pb}$ )\*–( $^{230}\text{Th}/^{232}\text{Th}$ ), which is interpreted as defining a Th/U ratio of the BSE [56] of 3.9–4.1. While this approach yields a similar BSE Th/U as other estimates, its major assumption that U–Th–Pb isotopic system has evolved as a closed system since 4.55 Ga is rather problematic.

## 2.7. Comparison of mass spectrometric data with older alpha spectrometry data

This study only assesses samples measured by mass spectrometric methods. It is important to note that despite large uncertainties associated with alpha spectrometric measurements of  $^{238}\text{U}/^{232}\text{Th}$  and  $^{230}\text{Th}/^{232}\text{Th}$  for many of the OIB samples, including the 1905 samples from Savaii [57], there is a good correspondence between the old alpha data and the newer mass

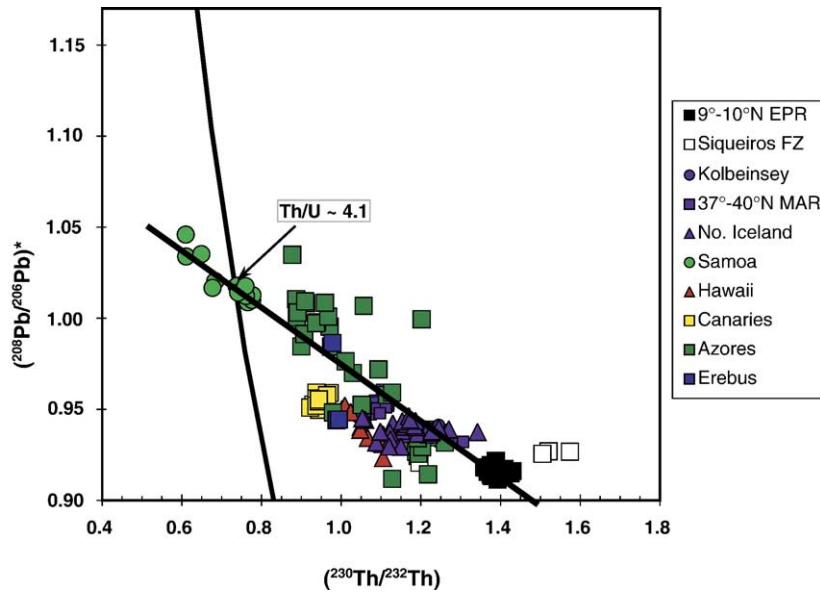


Fig. 9.  $(^{208}\text{Pb}/^{206}\text{Pb})^*$  versus  $(^{230}\text{Th}/^{232}\text{Th})$  for global data compilation. See Fig. 1 for data references. The data show a negative array that intersect a closed system Pb evolution line for the Bulk Silicate Earth (BSE) starting with an initial lead isotope system composition approximated by Canyon Diablo Troilite ( $T=4.55$  Ga). Th/U is calculated from  $(^{230}\text{Th}/^{232}\text{Th}) = (^{238}\text{U}/^{232}\text{Th})$  [i.e. the “closed” system is in radioactive equilibrium over the longterm}. This approach yields an intercept of 0.74–0.78 for  $(^{208}\text{Pb}/^{206}\text{Pb})^* - (^{230}\text{Th}/^{232}\text{Th})$ , which is interpreted as defining a Th/U ratio of the BSE [56] of 3.9–4.1.

spectrometric measurements. However, as has been pointed out by recent studies of Hawaiian and EPR basalts [5,10,11,26,27], the better precision of mass spectrometric methods provides a much finer resolution for assessing inter- and intra-suite variability in terms of melting processes and source variability. MORB also show a general coherence between alpha and mass spectrometry data. In fact, it was the alpha spectrometry data shown in Rubin et al. [2] which originally defined MORB’s distinct curvature toward higher  $(^{230}\text{Th}/^{232}\text{Th})$  and  $(^{238}\text{U}/^{232}\text{Th})$  at low and nearly constant  $^{87}\text{Sr}/^{86}\text{Sr}$ . However, this MORB alpha spectrometry data also have  $(^{230}\text{Th}/^{232}\text{Th})$  for lavas from the East Pacific Rise as high as 2.1, whereas the highest  $(^{230}\text{Th}/^{232}\text{Th})$  currently measured in MORBs by mass spectrometric methods is less than 1.6.

### 3. Conclusions

(1) The young Samoan samples have the lowest  $^{230}\text{Th}/^{232}\text{Th}$  and  $^{238}\text{U}/^{232}\text{Th}$  yet measured in oceanic basalts, consistent with the enriched nature of the EM2 mantle source. As such, the Samoan samples greatly extend the global correlations of  $(^{230}\text{Th}/^{232}\text{Th})$  and  $(^{238}\text{U}/^{232}\text{Th})$  with  $^{87}\text{Sr}/^{86}\text{Sr}$  and  $^{143}\text{Nd}/^{144}\text{Nd}$  and show that their functional form are hyperbolic rather than linear.

- (2) The historic Mt. Erebus samples, while not the end-member HIMU component, show intermediate  $(^{230}\text{Th}/^{232}\text{Th})$  and  $(^{238}\text{U}/^{232}\text{Th})$  consistent with their intermediate  $^{87}\text{Sr}/^{86}\text{Sr}$  and  $^{143}\text{Nd}/^{144}\text{Nd}$ .
- (3) Using a maximum likelihood non-linear regression technique, we show that to a first-order these correlations can, in part, be explained by simple two-component mixing of DMM and EM2, suggesting that Sm/Nd, Rb/Sr and Th/U behaved coherently during mantle differentiation over Earth’s history.
- (4) Our analysis shows that for the current global oceanic basalt database (MORB plus OIB)  $^{230}\text{Th}/^{232}\text{Th}$  is somewhat better correlated with the long-lived isotopes  $^{87}\text{Sr}/^{86}\text{Sr}$  and  $^{143}\text{Nd}/^{144}\text{Nd}$  than is  $^{238}\text{U}/^{232}\text{Th}$ . While this result has implications for the melting process, it is important to note that any such inferences are subject to the large uncertainties introduced by assuming that our limited database adequately characterizes the true variability of the unknown global distribution, and that the model misfit is not significantly influenced by variations due to mixing with additional mantle components (e.g., EM1, HIMU).
- (5) The global arrays of  $(^{230}\text{Th}/^{232}\text{Th})$  and  $(^{238}\text{U}/^{232}\text{Th})$  with Pb isotopic composition require four mixing components corresponding to the end-members that define the mantle tetrahedron

(DMM, HIMU, EM1 and EM2). For the current global oceanic basalt database, both ( $^{230}\text{Th}/^{232}\text{Th}$ ) and ( $^{238}\text{U}/^{232}\text{Th}$ ) behave more coherently with  $^{87}\text{Sr}/^{86}\text{Sr}$  and  $^{143}\text{Nd}/^{144}\text{Nd}$  than do the Pb isotopes (including  $^{208}\text{Pb}/^{206}\text{Pb}$ ). This observation suggests that the U–Pb isotopic system is “decoupled” from the other isotopic systems (e.g. Rb/Sr, Sm/Nd, U/Th) and that both ( $^{230}\text{Th}/^{232}\text{Th}$ ) and ( $^{238}\text{U}/^{232}\text{Th}$ ) are better proxies for the lavas’ Th/U source ratio than is  $^{208}\text{Pb}/^{206}\text{Pb}$ .

- (6) For all MORB suites and many OIB suites like Hawaii the variation of ( $^{230}\text{Th}/^{232}\text{Th}$ ) and ( $^{238}\text{U}/^{232}\text{Th}$ ) are greater than would be predicted by our best-fit two-component mixing models, suggesting that both  $^{230}\text{Th}$  in-growth (over the timescale of magma genesis) and net elemental U/Th fractionation (at low melt fractions) contribute to the observed ( $^{230}\text{Th}/^{238}\text{U}$ ) disequilibria in MORB and OIB.
- (7) The global oceanic basalt database show a strong inverse correlation between  $\sigma(^{230}\text{Th}/^{238}\text{U})/\sigma^{87}\text{Sr}/^{86}\text{Sr}$  and the degree of source enrichment (e.g.  $^{87}\text{Sr}/^{86}\text{Sr}$ ). The “depleted” MORB samples show the largest range of ( $^{230}\text{Th}/^{238}\text{U}$ ) and least variability in  $^{87}\text{Sr}/^{86}\text{Sr}$ , whereas the more “enriched” OIB suites show less variability in ( $^{230}\text{Th}/^{238}\text{U}$ ) but a larger range of  $^{87}\text{Sr}/^{86}\text{Sr}$ . We interpret this inverse relationship in terms of differences in the melting regimes beneath mid-ocean ridges and ocean islands.

## Acknowledgements

The authors thank Peter Kelemen, Tim Elliott, Nobu Shimizu, Ed Sklar, and Rob Sohn for enthusiastic and insightful discussions pertaining to this work. In particular, Rob Sohn is gratefully acknowledged for providing an early beta version of his code for the non-linear regressions and long discussions pertaining to its application. Constructive reviews by Ken Rubin and Craig Lundstrom improved the quality of this manuscript and are greatly appreciated. Editorial handling by Ken Farley was also valuable and appreciated. Support for this research was provided by NSF grants EAR-9909473, OCE-0137325, OCE-0422278 and OPP-01626900.

## References

- [1] C.J. Allegre, M. Condomines, Basalt genesis and mantle structure studies through Th-isotopic geochemistry, *Nature* 299 (1982) 21–24.

- [2] K.H. Rubin, J.D. MacDougall, Th–Sr isotopic relationships in MORB, *Earth and Planetary Science Letters* 114 (1992) 149–157.
- [3] M. Condomines, C. Hemond, C.J. Allegre, U–Th–Ra radioactive disequilibria and magmatic processes, *Earth and Planetary Science Letters* 90 (1988) 243–262.
- [4] C. Hemond, C.W. Devey, C. Chauvel, Source compositions and melting processes in the Society and Austral plumes (South Pacific Ocean): element and isotope (Sr, Nd, Pb, Th) geochemistry, *Chemical Geology* 115 (1994) 7–45.
- [5] K.W. Sims, D.J. DePaolo, M.T. Murell, W.S. Baldrige, S.J. Goldstein, D.A. Clague, Mechanisms of magma generation beneath Hawaii and mid-ocean ridges: uranium/thorium and samarium/neodymium isotopic evidence, *Science* 267 (1995) 508–512.
- [6] T. Elliott, Fractionation of U and Th during mantle melting: a reprise, *Chemical Geology* 139 (1997) 165–183.
- [7] M. Condomines, O. Sigmarrsson,  $^{238}\text{U}$ – $^{230}\text{Th}$  disequilibria and mantle melting processes: a discussion, *Chemical Geology* 162 (2000) 95–104.
- [8] B. Bourdon, K.W.W. Sims, U-series constraints on intraplate magmatism, in: G.M.H.B. Bourdon, C.C. Lundstrom, S.P. Turner (Eds.), *Uranium Series Geochemistry, Reviews in Mineralogy and Geochemistry*, vol. 52, 2003, pp. 215–253.
- [9] C. Lundstrom, Uranium-series disequilibria in mid-ocean ridge basalts: observations and models of basalt petrogenesis, in: G.M. H.B. Bourdon, C.C. Lundstrom, S.P. Turner (Eds.), *Uranium Series Geochemistry, Reviews in Mineralogy and Geochemistry*, vol. 52, 2003, pp. 175–212.
- [10] K.W.W. Sims, D.J. DePaolo, M.T. Murell, W.S. Baldrige, S. Goldstein, D.A. Clague, M. Jull, Porosity of the melting zone and variations in solid mantle upwelling rate beneath Hawaii: inferences from  $^{238}\text{U}$ – $^{230}\text{Th}$ – $^{226}\text{Ra}$  and  $^{235}\text{U}$ – $^{231}\text{Pa}$  disequilibria, *Geochimica et Cosmochimica Acta* 63 (1999) 4119–4138.
- [11] K.W.W. Sims, S.J. Goldstein, J. Blichert-Toft, M.R. Perfit, P. Kelemen, D.J. Fornari, P. Michael, M.T. Murrell, S.R. Hart, D.J. DePaolo, G. Layne, L. Ball, M. Jull, J.F. Bender, Chemical and isotopic constraints on the generation and transport of magma beneath the East Pacific Rise, *Geochimica et Cosmochimica Acta* 66 (2002) 3481–3504.
- [12] A. Zindler, S. Hart, Chemical geodynamics, *Annual Review of Earth and Planetary Sciences* 14 (1986).
- [13] S.R. Hart, E.H. Hauri, L.A. Oschmann, J.A. Whitehead, Mantle plumes and entrainment: isotopic evidence, *Science* 256 (1992) 517–520.
- [14] R.K. Workman, S.R. Hart, M. Jackson, M. Regelous, K.A. Farley, J. Blusztajn, M. Kurz, H. Staudigel, Recycled metasomatized lithosphere as the origin of the enriched mantle II (EM2) endmember: evidence from the Samoan volcanic chain, *Geochemistry, Geophysics, Geosystems* 5 (2004) Art. No. Q04008.
- [15] B. Bourdon, A. Zindler, T. Elliott, C. Langmuir, Constraints on mantle melting at mid-ocean ridges from global  $^{238}\text{U}$ – $^{230}\text{Th}$  disequilibrium data, *Nature* 384 (1996) 231–235.
- [16] S.J. Goldstein, M.T. Murrell, D.R. Janeky, Th and U isotopic systematics of basalts from the Juan de Fuca and Gorda Ridges by mass spectrometry, *Earth and Planetary Science Letters* 96 (1989) 134–146.
- [17] S.J. Goldstein, M.T. Murrell, R.W. Williams,  $^{231}\text{Pa}$  and  $^{230}\text{Th}$  chronology of mid-ocean ridge basalts, *Earth Planetary Science Letters* 115 (1993) 151–159.
- [18] B. Bourdon, C.H. Langmuir, A. Zindler, Ridge-hotspot interaction along the Mid-Atlantic Ridge between 37–30° and 40–30°N:

- the U–Th disequilibrium evidence, *Earth Planetary Science Letters* 142 (1996) 175–189.
- [19] C. Lundstrom, J. Gill, Q. Williams, M.R. Perfit, Mantle melting and basalt extraction by equilibrium porous flow, *Science* 270 (1995) 1958–1961.
- [20] C.C. Lundstrom, J. Gill, Q. Williams, B.B. Hanan, Investigating solid mantle upwelling beneath mid-ocean ridges using U-series disequilibria: II. A local study at 33°S mid-Atlantic Ridge, *Earth and Planetary Science Letters* 157 (1998) 167–181.
- [21] C.C. Lundstrom, D.E. Sampson, M.R. Perfit, J. Gill, Q. Williams, Insight into mid-ocean ridge basalt petrogenesis: U-series disequilibria from the Siqueiros Transform, Lamont Seamounts, and East Pacific Rise, *Journal of Geophysical Research* 104 (1999) 13035–13048.
- [22] D.W. Peate, C.J. Hawkesworth, P.W. van Calsteren, R.N. Taylor, B.J. Murton,  $^{238}\text{U}$ – $^{230}\text{Th}$  constraints on mantle upwelling and plume–ridge interaction along the Reykjanes Ridge, *Earth and Planetary Science Letters* 187 (2001) 259–272.
- [23] F.J.I. Tepley, C.C. Lundstrom, K.W.W. Sims, R. Hekinian, U-series disequilibria in MORB from the Garrett Transform and implications for mantle melting, *Earth and Planetary Science Letters* 223 (2004) 79–97.
- [24] K.W. Sims, N. Mattioli, T. Elliott, P. Kelemen, D.J. DePaolo, D. F. Mertz, C. Devey, M.T. Murrell,  $^{238}\text{U}$  and  $^{230}\text{Th}$  excesses in Kolbeinsey ridge basalts, *Eos Transactions AGU* 82 (47) (2001) Fall Meeting Supplement.
- [25] M.E. Sturm, S.J. Goldstein, E.M. Klein, J.A. Karson, M.T. Murrell, Uranium-series age constraints on lavas from the axial valley of the Mid-Atlantic Ridge, MARK area, *Earth and Planetary Science Letters* 181 (2000) 61–70.
- [26] A.S. Cohen, O.N.R. K., Melting rates beneath Hawaii: evidence from uranium series isotopes in recent lavas, *Earth and Planetary Science Letters* 120 (1993) 169–175.
- [27] A.J. Pietruszka, K.H. Rubin, M.O. Garcia,  $^{226}\text{Ra}$ – $^{230}\text{Th}$ – $^{238}\text{U}$  disequilibria of historic Kilauea lavas (1790–1982) and the dynamics of mantle melting within the Hawaiian plume, *Earth and Planetary Science Letters* 186 (2001) 15–31.
- [28] A. Stracke, A. Zindler, V.J.M. Salters, D. McKenzie, K. Gronvold, The dynamics of melting beneath the Heistareykir, northern Iceland, *Geochemistry, Geophysics, Geosystems* 4 (2003) 8513, doi:10.1029/2002GC000347.
- [29] T.F. Kokfelt, K. Hoernle, F. Hauff, Upwelling and melting of the Iceland plume from radial variation of  $^{238}\text{U}$ – $^{230}\text{Th}$  disequilibria in postglacial volcanic rocks, *Earth and Planetary Science Letters* 214 (2003) 167.
- [30] O. Sigmarsson, S. Carn, J.C. Carracedo, Systematics of U-series nuclides in primitive lavas from the 1730–36 eruption in Lanzarote, Canary Islands, and the implications for the role of garnet pyroxenite during oceanic basalt formation, *Earth and Planetary Science Letters* 162 (1998) 1337–1351.
- [31] L.E. Thomas, C.J. Hawkesworth, P. Van Calsteren, S.P. Turner, N.W. Rodgers, Melt generation beneath ocean islands: a U–Th–Ra isotope study from Lanzarote in the Canary Islands, *Geochimica et Cosmochimica Acta* 63 (1999) 4081–4099.
- [32] C.C. Lundstrom, K. Hoernle, J. Gill, U-series disequilibria in volcanic rocks from the Canary Islands: plume versus lithospheric melting, *Geochimica et Cosmochimica Acta* 67 (2003) 4153–4177.
- [33] S. Turner, C. Hawkesworth, N. Rodgers, P. King, U–Th disequilibria and ocean island basalt generation in the Azores, *Chemical Geology* 139 (1997) 145–164.
- [34] C. Claude-Ivanaj, B. Bourdon, C.J. Allegre, Ra–Th–Sr isotope systematics in Grande Comore Island: a case study of plume–lithosphere interaction, *Earth and Planetary Science Letters* 164 (1998) 99–117.
- [35] E. Widom, R.W. Carlson, J.B. Gill, H.U. Schmincke, Th–Sr–Nd–Pb isotope and trace element evidence for the origin of the Sao Miguel, Azores, enriched mantle source, *Chemical Geology* 140 (1997) 49–68.
- [36] D. Landwehr, J. Blundy, E. Chamorro-Perez, E. Hill, B. Wood, U-series disequilibria generated by partial melting of spinel lherzolite, *Earth and Planetary Science Letters* 188 (2001) 329–348.
- [37] P. Beattie, Uranium–thorium disequilibria and partitioning on melting of garnet peridotite, *Nature* 363 (1993) 63–65.
- [38] T.Z. LaTourette, A.K. Kennedy, G.J. Wasserburg, U–Th fractionation by garnet-evidence for a deep source and rapid rise by oceanic basalts, *Science* 261 (1993) 739–742.
- [39] V.J.M. Salters, J. Longhi, Trace element partitioning during the initial stages of melting beneath mid-ocean ridges, *Earth and Planetary Science Letters* 166 (1999) 15–30.
- [40] R.A. Sohn, A general inversion for end member ratios in binary mixing, *Geochemistry, Geophysics, Geosystems* 6 (2005).
- [41] D. McKenzie,  $^{230}\text{Th}$ – $^{238}\text{U}$  disequilibrium and the melting processes beneath ridge axes, *Earth and Planetary Science Letters* 72 (1985) 149–157.
- [42] M. Spiegelman, T. Elliott, Consequences of melt transport for U-series disequilibrium in young lavas, *Earth and Planetary Science Letters* 118 (1993) 1–20.
- [43] M. Spiegelman, P.B. Kelemen, Extreme chemical variability as a consequence of channelized melt transport, *Geochemistry, Geophysics, Geosystems* 4 (2003) 18.
- [44] T. Elliott, A. Zindler, B. Bourdon, Exploring the kappa conundrum: the role of recycling in the lead isotope evolution of the mantle, *Earth and Planetary Science Letters* 169 (1999) 129–145.
- [45] M. Tatsumoto, Genetic relationships of oceanic basalts as indicated by Pb isotopes, *Science* 153 (1966) 1094–1101.
- [46] S.J.G. Galer, R.K. O’Nions, Residence time of thorium, uranium and lead in the mantle with implications for mantle convection, *Nature* 316 (1985) 778–782.
- [47] K.W.W. Sims, D.J. DePaolo, Inferences about mantle magma sources from incompatible element concentration ratios in oceanic basalts, *Geochimica et Cosmochimica Acta* 61 (4) (1997) 765–784.
- [48] M. Spiegelman, T. Elliott, Consequences of melt transport for uranium series disequilibrium in young lavas, *Earth and Planetary Science Letters* 118 (1993) 1–20.
- [49] M. Jull, P. Kelemen, K.W.W. Sims, Melt migration and uranium series disequilibria: the combined effect of porous and conduit flow, *Geochimica et Cosmochimica Acta* 66 (23) (2003) 4133–4148.
- [50] N.H. Sleep, Hotspots and mantle plumes: some phenomenology, *Journal of Geophysical Research* 95 (1990) 6715–6736.
- [51] F. Chabaux, C.J. Allegre,  $^{238}\text{U}$ – $^{230}\text{Th}$ – $^{226}\text{Ra}$  disequilibria in volcanics—a new insight into melting conditions, *Earth and Planetary Science Letters* 126 (1994) 61–74.
- [52] M.M. Hirschmann, E.M. Stolper, A possible role for garnet pyroxenite in the origin of the “garnet signature” in MORB, *Contributions to Mineralogy and Petrology* 124 (1996) 185–208.
- [53] M. Pertermann, M.M. Hirschmann, Partial melting experiments on a MORB-like pyroxenite between 2 and 3 GPa: constraints on the presence of pyroxenite in basalt source regions from solidus

- location and melting rate, *Journal of Geophysical Research* 108 (2003) 16.
- [54] R.K. Workman, S.R. Hart, Major and trace element composition of the depleted MORB mantle (DMM), *Earth and Planetary Science Letters* 231 (2005) 53–72.
- [55] M.a.R.W.C. Boyet,  $^{142}\text{Nd}$  evidence for early ((4.53 Ga) global differentiation of the silicate earth, *Science* 309 (2005) 576–580.
- [56] C.J. Allegre, B. Dupre, E. Lewin, Thorium/uranium ratio of the Earth, *Chemical Geology* 56 (1986) 219–227.
- [57] S. Newman, R.C. Finkel, J.D. Macdougall, Comparison of  $^{230}\text{Th}$ – $^{238}\text{U}$  disequilibrium systematics in lavas from three hot spot regions: Hawaii, Prince Edward and Samoa, *Geochimica et Cosmochimica Acta* 48 (1984) 315–324.
- [58] J.D. Woodhead, Extreme HIMU in an oceanic setting: the geochemistry of Mangaia Island (Polynesia), and temporal evolution of the Cook-Austral hotspot, *Journal of Volcanology and Geothermal Research* 72 (1996) 1–19.
- [59] E.H. Hauri, S.R. Hart, Re–Os isotope systematics of HIMU and EMII oceanic island basalts from the south Pacific Ocean, *Earth and Planetary Science Letters* 114 (1993) 353–371.
- [60] J. Eisele, M. Sharma, S.J.G. Galer, J. Blichert-Toft, C.W. Devey, A.W. Hofmann, The role of sediment recycling in EM-I inferred from Os, Pb, Hf, Nd, Sr isotope and trace element systematics of the Pitcairn hotspot, *Earth and Planetary Science Letters* (2002) 197–212.
- [61] W. Todt, R.A. Cliff, A. Hanser, A.W. Hofmann, Evaluation of a  $^{202}\text{Pb}$ – $^{205}\text{Pb}$  double spike for high-precision lead isotope analysis, in: S.R.B. Hart, A. (Eds.), *Earth Processes Reading the Isotope Code 95*, AGU, 1996, pp. 429–437.
- [62] W.M. White, F. Albarede, P. Telouk, High-precision analysis of Pb isotope ratios using multicollector ICP-MS, *Chemical Geology* 167 (2000) 270–275.
- [63] G. Layne, K.W.W. Sims, Secondary ion mass spectrometry for the measurement of  $^{232}\text{Th}/^{230}\text{Th}$  in volcanic rocks, *International Journal of Mass Spectrometry* 203 (2000) 187–198.
- [64] R.A. Sohn, W. Menke, Application of maximum likelihood and bootstrap methods to nonlinear curve-fit problems in geochemistry, *G-cubed* 3 (2002), doi:10.1029/2001GC000253.